

# Elevated Tropospheric Iodine over the Central Continental United States: Is Iodine a Major Oxidant of Atmospheric Mercury?

Christopher Francis Lee<sup>1</sup>, Tyler Eligar<sup>2</sup>, Liji M David<sup>3</sup>, Taylor Yukai Wilmot<sup>4</sup>, Mago Reza<sup>1</sup>, Noah Hirshorn<sup>4</sup>, Ian B. McCubbin<sup>4</sup>, Viral Shah<sup>5</sup>, John C. Lin<sup>4</sup>, Seth Lyman<sup>6</sup>, A. Gannet Hallar<sup>4</sup>, Lynne E. Gratz<sup>7</sup>, and Rainer Volkamer<sup>1</sup>

<sup>1</sup>University of Colorado Boulder

<sup>2</sup>Utah State University

<sup>3</sup>Ramboll

<sup>4</sup>University of Utah

<sup>5</sup>NASA Global Modeling and Assimilation Office and SSAI

<sup>6</sup>usu

<sup>7</sup>Reed College

March 25, 2024

## Abstract

Previous efforts to measure atmospheric iodine have focused on marine and coastal regions. We report the first ground-based tropospheric iodine monoxide (IO) radical observations over the central continental United States. Throughout April 2022, IO columns above Storm Peak Laboratory, Colorado (3220 m.a.s.l.) ranged from  $0.7 \pm 0.5$  to  $3.6 \pm 0.5 \times 10^{12}$  (average:  $1.9 \times 10^{12}$  molec cm $^{-2}$ ). IO was consistently elevated in air masses transported from over the Pacific Ocean. The observed IO columns were up to three times higher and the range was larger than predicted by a global model, which warrants further investigation into iodine sources, sinks, ozone loss, and particle formation. IO mixing ratios increased with altitude. At the observed levels, iodine may be competitive with bromine as an oxidant of elemental mercury at cold temperatures typical of the free troposphere (4–12 km; <260 K). Iodine-induced mercury oxidation is missing in atmospheric models, understudied, and helps explain model underestimation of oxidized mercury measurements.

## Hosted file

Lee\_et\_al\_2024\_manuscript.docx available at <https://authorea.com/users/756965/articles/729048-elevated-tropospheric-iodine-over-the-central-continental-united-states-is-iodine-a-major-oxidant-of-atmospheric-mercury>

## Hosted file

Lee\_et\_al\_2024\_SI-text.docx available at <https://authorea.com/users/756965/articles/729048-elevated-tropospheric-iodine-over-the-central-continental-united-states-is-iodine-a-major-oxidant-of-atmospheric-mercury>

1  
2 **Elevated Tropospheric Iodine over the Central Continental United States: Is Iodine a**  
3 **Major Oxidant of Atmospheric Mercury?**

4 C. F. Lee<sup>1,2</sup>, T. Elgiar<sup>3</sup>, L. M. David<sup>3,+</sup>, T. Y. Wilmot<sup>4</sup>, M. Reza<sup>1,2</sup>, N. Hirshorn<sup>4,%</sup>, I. B.  
5 McCubbin<sup>4</sup>, V. Shah<sup>5,#</sup>, J. C. Lin<sup>4</sup>, S. N. Lyman<sup>3,6</sup>, A. G. Hallar<sup>4</sup>, L. E. Gratz<sup>7,\*</sup>, and R.  
6 Volkamer<sup>1,2</sup>

7 <sup>1</sup>Department of Chemistry, University of Colorado Boulder, Boulder, CO, USA

8 <sup>2</sup>Cooperative Institute for Research in Environmental Sciences, Boulder, CO, USA

9 <sup>3</sup>Bingham Research Center, Utah State University, Vernal, UT, USA

10 <sup>4</sup>Department of Atmospheric Sciences, University of Utah, Salt Lake City, UT, USA

11 <sup>5</sup>School of Engineering and Applied Sciences, Harvard University, Cambridge, MA, USA

12 <sup>6</sup>Department of Chemistry & Biochemistry, Utah State University, Logan, UT, USA

13 <sup>7</sup>Environmental Studies Program, Colorado College, Colorado Springs, CO, USA

14 Corresponding author: Rainer Volkamer ([rainer.volkamer@colorado.edu](mailto:rainer.volkamer@colorado.edu))

15 <sup>+</sup>Current affiliation: Ramboll, Fort Collins, CO, USA

16 <sup>%</sup>Current affiliation: Ramboll, New York, NY, USA

17 <sup>#</sup>Current affiliation: Science Systems and Applications, Inc., Lanham, MD, USA

18 \*Current affiliation: Department of Chemistry and Environmental Studies Program, Reed  
19 College, Portland, OR, USA

20 **Key Points:**

- 21 • Measurements of iodine monoxide radicals at Storm Peak Laboratory are up to three  
22 times higher than predicted by GEOS-Chem.
- 23 • IO tropospheric column variability is significant and highlights a need to better  
24 understand sources and sinks of free tropospheric iodine.
- 25 • Iodine rivals bromine as an oxidant of mercury in the upper troposphere; iodine-mercury  
26 chemistry is understudied and missing in atmospheric models.

## 27 Abstract

28 Previous efforts to measure atmospheric iodine have focused on marine and coastal regions. We  
29 report the first ground-based tropospheric iodine monoxide (IO) radical observations over the  
30 central continental United States. Throughout April 2022, IO columns above Storm Peak  
31 Laboratory, Colorado (3220 m.a.s.l.) ranged from  $0.7 \pm 0.5$  to  $3.6 \pm 0.5 \times 10^{12}$  (average:  $1.9 \times 10^{12}$   
32 molec cm $^{-2}$ ). IO was consistently elevated in air masses transported from over the Pacific Ocean.  
33 The observed IO columns were up to three times higher and the range was larger than predicted  
34 by a global model, which warrants further investigation into iodine sources, sinks, ozone loss,  
35 and particle formation. IO mixing ratios increased with altitude. At the observed levels, iodine  
36 may be competitive with bromine as an oxidant of elemental mercury at cold temperatures  
37 typical of the free troposphere (4–12km; <260K). Iodine-induced mercury oxidation is missing  
38 in atmospheric models, understudied, and helps explain model underestimation of oxidized  
39 mercury measurements.

## 40 Plain Language Summary

41 Halogens such as chlorine, bromine, and iodine are highly reactive gases that participate in  
42 atmospheric chemistry, including ozone destruction, particle formation, modification of  
43 greenhouse gas lifetime (i.e. methane, dimethylsulfide), and the oxidation of elemental mercury.  
44 Iodine mainly enters the atmosphere from oceans; therefore, past measurements of atmospheric  
45 iodine have focused on marine and polar regions. This study describes the first lower  
46 atmospheric measurements of iodine monoxide (IO) radicals at a remote mountaintop site in the  
47 central continental United States. These measurements indicate that the concentration of IO  
48 radicals showed a large range over the course of one month and reached levels up to three times  
49 higher than predicted by a global atmospheric chemistry model. These observations suggest that  
50 our understanding of the iodine sources and sinks to the free troposphere may be incomplete.  
51 Moreover, we suggest that iodine's contribution to ozone destruction and mercury chemistry  
52 may be underestimated; in particular, iodine may be competitive with bromine in the oxidation  
53 of elemental mercury in the free troposphere.

## 54 1 Introduction

55 Atmospheric iodine destroys ozone (Read et al., 2008; Saiz-Lopez et al., 2012, 2014;  
56 Sherwen et al., 2017; Koenig et al., 2020, 2021), forms new particles (O'Dowd et al. 2002; Sipilä  
57 et al., 2016; Baccarini et al., 2020; He et al., 2021; Gómez Martín et al., 2022; Finkenzeller et al.,  
58 2023), and modifies atmospheric oxidative capacity (Sherwen et al., 2016a, 2016b). Iodine  
59 mainly enters the atmosphere in inorganic gaseous form (HOI, I<sub>2</sub>) through reaction with ozone at  
60 the ocean surface (Carpenter et al., 2013; MacDonald et al., 2014; Wang et al., 2021), with  
61 smaller sources from organic iodine species (Bell et al., 2002; Sive et al., 2007; Jones et al., 2010;  
62 Ordóñez et al., 2012; Wang et al., 2021), windblown dust (Williams et al., 2007; Koenig et al.,  
63 2021), and volcanic eruptions (Schönhardt et al., 2017). Tree ring and ice core records indicate  
64 that atmospheric iodine has increased threefold since 1950, which is attributed to increased  
65 anthropogenic surface ozone pollution resulting in increased marine iodine emissions (Legrand  
66 et al., 2018; Cuevas et al., 2018; Zhao et al. 2019).

67 Most of our knowledge about the global distribution of atmospheric iodine is from  
68 measurements of iodine monoxide (IO) radicals in the marine boundary layer (Aliche et al.,  
69 1999; Allan et al., 2000; Whalley et al., 2007; Furneaux et al., 2010; Coburn et al., 2011;

70 Mahajan et al., 2012; Gómez Martín et al., 2013; Großmann et al., 2013; Prados-Roman et al.,  
71 2015; Inamdar et al., 2020; Takashima et al., 2022) and at high latitudes (Wittrock et al., 2000;  
72 Frieß et al., 2010; Mahajan et al., 2010; Schönhardt et al., 2012, 2017). Recent evidence of IO in  
73 the free troposphere is limited to measurements over oceans (Puentedura et al., 2012; Dix et al.,  
74 2013; Wang et al., 2015; Volkamer et al., 2015; Koenig et al., 2021). IO in the tropical transition  
75 layer (Volkamer et al., 2015) and lower stratosphere (Koenig et al., 2020) suggests that iodine is  
76 globally distributed. To our knowledge, there is no previous ground-based measurement of  
77 tropospheric IO over the continental United States. The only previous attempt to measure IO  
78 from the continental U.S. was by Wennberg et al. (1997), who measured IO slant column  
79 densities (SCDs) during three sunrises at Kitt Peak, Arizona, with a solar geometry that  
80 maximized sensitivity to stratospheric IO but minimized sensitivity to tropospheric IO; they did  
81 not attempt to quantify tropospheric IO. Therefore, tropospheric IO over the center of the  
82 continental U.S. is unconstrained by ground-based measurements.

83 Mountaintop Multi-AXis Differential Optical Absorption Spectroscopy (MAX-DOAS) is  
84 well-suited for tropospheric IO measurements because it maximizes measurement sensitivity by  
85 minimizing aerosol scattering effects, provides access to the free troposphere due to the extended  
86 spatial scale (tens of kilometers) of the measurement light path, and enables cost-effective long-  
87 term measurements compared to airborne campaigns. Mountaintop MAX-DOAS has been  
88 successfully employed for IO measurements in the marine free troposphere (Puentedura et al.,  
89 2012).

90 The role of iodine radicals as oxidants of atmospheric mercury is understudied. Mercury  
91 enters the atmosphere mainly in gaseous elemental form,  $\text{Hg}^0_{(\text{g})}$ , where it is oxidized into short-  
92 lived  $\text{Hg}^{\text{I}}(\text{X})_{(\text{g})}$  species ( $\text{X} = \text{Br}, \text{OH}, \text{Cl}$ ) and subsequently reacts with ozone or other secondary  
93 oxidants to form  $\text{Hg}^{\text{II}}_{(\text{g})}$  species (Dibble et al., 2020; Shah et al., 2021; Castro et al., 2022). The  
94 oxidation of  $\text{Hg}^0_{(\text{g})}$  by atmospheric iodine radicals has been deemed unimportant due to the low  
95 amounts of tropospheric iodine and the much faster thermal decomposition of  $\text{Hg}^{\text{I}}(\text{I})_{(\text{g})}$  compared  
96 to  $\text{Hg}^{\text{I}}(\text{Br})_{(\text{g})}$  (Goodsite et al., 2004; Shepler et al., 2005; Cremer et al., 2008). Accordingly, the  
97 latest implementation of atmospheric mercury chemistry in the GEOS-Chem model does not  
98 include reactions involving iodine (Shah et al., 2021). However, mercury measurements in  
99 aerosols are empirically correlated with iodine (Murphy et al., 2006). Additionally, the fast,  
100 barrierless reaction of  $\text{Hg}^{\text{I}}$  species with ozone (Saiz-Lopez et al., 2020) can compete with the  
101 thermal decomposition of  $\text{Hg}^{\text{I}}(\text{I})_{(\text{g})}$ , prompting us to re-evaluate the importance of iodine as an  
102  $\text{Hg}^0_{(\text{g})}$  oxidant.

103 Here we present one month (April 1–30, 2022) of MAX-DOAS measurements of IO,  
104  $\text{H}_2\text{O}$ ,  $\text{NO}_2$ , and  $\text{HCHO}$  tropospheric vertical column densities ( $\text{VCD}_{\text{trop}}$ ) and volume mixing  
105 ratios at instrument altitude ( $\text{VMR}_{\text{instr}}$ ) alongside co-located in-situ measurements of  $\text{Hg}^0_{(\text{g})}$  and  
106  $\text{Hg}^{\text{II}}$  at a remote mountaintop observatory in the central continental U.S. Section 2 describes the  
107 measurement site and methods. Section 3 presents the first ground-based observational constraint  
108 on tropospheric IO over the central continental U.S., explores correlations, and compares  
109 observations with a global model. Section 4 uses the observations to constrain a box model of  
110 gas-phase mercury chemistry to investigate the relevance of iodine radicals for  $\text{Hg}^0_{(\text{g})}$  oxidation  
111 and discusses atmospheric implications.

112 **2 Methods**113 **2.1 Storm Peak Laboratory**

114 Storm Peak Laboratory (SPL) is a mountaintop observatory on top of the continental  
115 divide in the Rocky Mountains in northwestern Colorado (3220 m.a.s.l, 40.455°N, 106.745°W).  
116 SPL has been an atmospheric research station since the 1980's (Borys & Wetzel, 1997; Hallar et  
117 al., 2016) and has been previously used for atmospheric mercury measurements (Obrist et al.,  
118 2008; Fain et al., 2009). All measurements presented here were conducted at SPL from April 1–  
119 30, 2022.

120 **2.1.1 CU MAX-DOAS**

121 The University of Colorado MAX-DOAS (CU MAX-DOAS) instrument (Coburn et al.,  
122 2011, 2016) measured ultraviolet-visible scattered-light solar spectra at different elevation angles  
123 in a single azimuthal viewing direction. Trace gas differential slant column densities (dSCDs)  
124 were retrieved from solar spectra using the DOAS method (Platt & Stutz, 2008; Van Roozendael,  
125 2021). A cloud-free zenith reference spectrum (Gielen et al., 2014; Wagner et al., 2014) on April  
126 6, 2022 at 18:00 UTC was used for all DOAS retrievals; fit settings are in Tables S1 & S2. IO,  
127 H<sub>2</sub>O, HCHO, and O<sub>2</sub>-O<sub>2</sub> dSCDs were converted into SCDs by adding the trace gas SCD in the  
128 reference spectrum (SCD<sub>ref</sub>); past studies have shown that accounting for SCD<sub>ref</sub> maximizes  
129 sensitivity in the free troposphere (Hendrick et al., 2007; Coburn et al., 2016) and avoids bias in  
130 the retrieval of columns and profiles (Volkamer et al., 2015). For NO<sub>2</sub>, the stratospheric signal  
131 was removed by subtracting the zenith dSCDs from the off-axis dSCDs. A linear optimal  
132 estimation algorithm (Rodgers, 2004) was used to retrieve IO, NO<sub>2</sub>, H<sub>2</sub>O, and HCHO VCD<sub>trop</sub>  
133 and VMR<sub>instr</sub> from the measured SCDs (zenith-subtracted dSCDs for NO<sub>2</sub>). Instrument and  
134 retrieval details are in Text S1.

135 **2.1.2 Dual-channel mercury system**

136 A cation-exchange membrane-based dual-channel system to measure Hg<sup>0</sup><sub>(g)</sub> and Hg<sup>II</sup>  
137 (Lyman et al., 2020; Elgiar et al., submitted) pulled sample air through a heated PTFE Teflon-  
138 coated inlet with an elutriator and particle impactor (2.5 μm cut point), 50 cm of heated PFA  
139 Teflon line, to two separate measurement channels. A Tekran 2537X Hg vapor analyzer sampled  
140 from each channel sequentially. One channel included a series of two in-series cation exchange-  
141 membranes that have been shown to pass Hg<sup>0</sup><sub>(g)</sub> and retain Hg<sup>II</sup> (Miller et al., 2019); the other  
142 channel included a thermal converter that converted total atmospheric Hg to Hg<sup>0</sup><sub>(g)</sub>. Hg<sup>II</sup> was  
143 calculated as the difference between the two channels every ten minutes.. The dual-channel  
144 system had a 1-hour Hg<sup>II</sup> detection limit less than 15 pg m<sup>-3</sup>; total Hg and Hg<sup>0</sup><sub>(g)</sub> are assumed to  
145 be similar. A NIST-traceable permeation tube-based calibrator was used to add Hg<sup>0</sup><sub>(g)</sub> and HgBr<sub>2</sub>  
146 to the inlet of the dual-channel system while it sampled ambient air, and the system recovered  
147 97±4% and 100±9%, respectively (mean ± standard deviation). The dual-channel system is  
148 described in detail in Elgiar et al. (submitted).

149 **2.2 Model tools**150 **2.2.1 GEOS-Chem**

151        The GEOS-Chem 3-D atmospheric chemistry model was used to simulate (1) oxidant  
152 fields and (2) mercury chemistry as described in Shah et al. (2021). Details are in Text S2. April  
153 2022 daytime averages of GEOS-Chem oxidant fields and Hg<sup>0</sup> were used to constrain the gas-  
154 phase mercury box model described in Section 2.2.3.

155        2.2.2 HYSPLIT-STILT

156        The Hybrid Single-Particle Lagrangian Integrated Trajectory (HYSPLIT) model coupled  
157 to the Stochastic Time-Inverted Lagrangian Transport Model (STILT; Lin et al., 2003; Loughner  
158 et al., 2021) was used to simulate air mass origin at SPL. One thousand 24-hour back trajectories  
159 were initiated at each of multiple altitudes (5 m, 2 km, 4 km, 6 km, 10 km above ground level) at  
160 SPL every 3 hours from April 1–30, 2022. At each initial altitude, the one thousand back-  
161 trajectories were averaged in three dimensions (latitude, longitude, altitude) to calculate a single  
162 back trajectory every three hours (Figure 1). Details are in Text S4.

163        2.2.3 Mercury box model

164        The Framework for 0-D Atmospheric Modeling (F0AM; Wolfe et al, 2016) version 4.2.2  
165 was used to simulate gas-phase mercury chemistry in 1 km layers from the surface at 2 km to 12  
166 km. GEOS-Chem April 2022 daytime averages were used to constrain oxidant fields and Hg<sup>0</sup>;  
167 iodine radicals were scaled to the average observed IO column (Text S3). The reaction  
168 mechanism used is based on Shah et al. (2021) with three significant differences; first, reactions  
169 involving I & IO were added analogously to reactions involving Br & BrO (Saiz-Lopez et al.,  
170 2018); second, the reaction coefficient used for  $Hg^{I(X)} + O_3 \rightarrow Hg^{II(X)(O)} + O_2$  was the value for  
171 a barrierless reaction reported in Saiz-Lopez et al. (2020); third, only gas-phase reactions are  
172 treated here, as the goal is to examine the relative contributions of Br, OH, and I to Hg<sup>0(g)</sup>  
173 oxidation rates. Hg<sup>II(g)</sup> deposition and particle-phase partitioning is not the focus of this study and  
174 deemed independent of Hg<sup>II(g)</sup> chemical identity (Shah et al., 2021). Sensitivity studies were  
175 performed varying the rate for  $Hg^0 + I + M \rightarrow Hg^I(I) + M$ , where a) Hg<sup>I(I)</sup> forms at the same rate  
176 as Hg<sup>I(Br)</sup> and b) Hg<sup>I(I)</sup> forms at the rate calculated by Goodsite et al. (2004). The bond strength  
177 of Hg<sup>I(I)</sup> is uncertain (Goodsite et al., 2004; Shepler et al., 2005; Cremer et al., 2008), and  
178 sensitivity studies were performed varying the decomposition rate for  $Hg^I(I) + M \rightarrow Hg^0 + I +$   
179 M, where a) Hg<sup>I(I)</sup> dissociates at the same rate as Hg<sup>I(OH)</sup>, b) 10 times faster, and c) 100 times  
180 faster. Box model output was extracted at fifteen minutes, after gas-phase equilibrium was  
181 reached (Figure S3). The complete reaction mechanism is in Tables S5 and S6.

182        2.2.4 Radiative transfer model

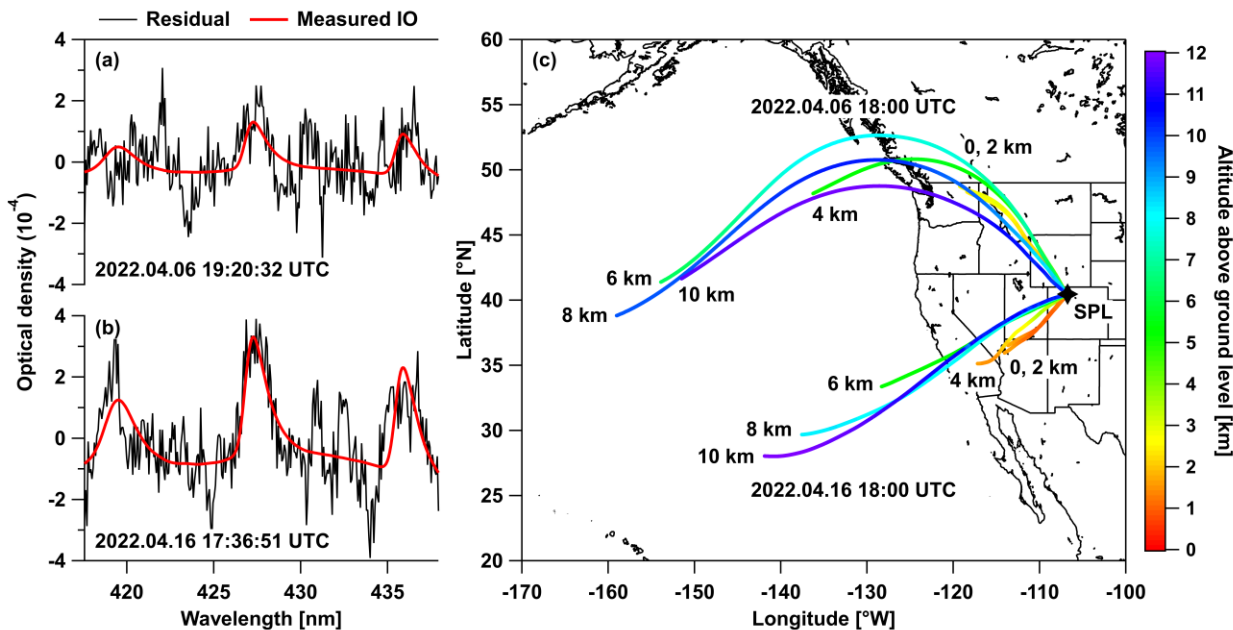
183        The 3D Monte Carlo Atmospheric Radiative Transfer Inversion Model (McArtim3;  
184 Deutschmann et al., 2011) was used to calculate weighting functions for trace gas profile  
185 inversions. Model settings are in Table S2. Weighting functions were calculated in a Rayleigh  
186 atmosphere using April 2022 average daytime temperature and pressure profiles from ECMWF  
187 CAMS reanalysis (Inness et al., 2019) and empirically scaled to match the measured O<sub>2</sub>-O<sub>2</sub> SCD  
188 for each spectrum. This approach uses the known O<sub>2</sub>-O<sub>2</sub> vertical profile to account for the  
189 effects of terrain and temporal atmospheric state variability (temperature, pressure, weak  
190 aerosols) on the measured photon path distribution (Spinei et al., 2015; Ortega et al., 2016;  
191 Wagner et al., 2019; Tirpitz et al., 2021; see Text S1).

192 **3 Results**

193 Here, IO observations are described, compared with GEOS-Chem simulations, and  
 194 examined alongside co-located observations of air mass tracers for atmospheric dynamics ( $\text{H}_2\text{O}$ ),  
 195 pollution ( $\text{NO}_2$ ), total oxidative capacity ( $\text{HCHO}$ ), and mercury oxidation ( $\text{Hg}_{(\text{g})}^0, \text{Hg}_{(\text{g})}^{\text{II}}$ ). Pearson  
 196 correlation coefficients ( $R$ ) of less than 0.20 are referred to as having no correlation;  $R$  is  
 197 reported alongside its standard error. Averages are reported alongside standard deviations.

198 **3.1 Detection of IO in the continental free troposphere**

199 IO concentrations above the detection limit were consistently observed throughout the  
 200 month; spectral proofs are shown in Figure 1. On April 16, the day with the highest IO signal, IO  
 201 dSCDs of up to  $(2.2 \pm 0.4) \times 10^{13}$  and  $(1.6 \pm 0.1) \times 10^{13}$  molec  $\text{cm}^{-2}$  were observed in the limb  
 202 ( $\text{EA}=0^\circ$ ) and zenith ( $\text{EA}=90^\circ$ ) geometries, respectively. On April 6, the day with the lowest IO  
 203 signal, IO dSCDs of up to  $(1.4 \pm 0.4) \times 10^{13}$  and  $(0.6 \pm 0.1) \times 10^{13}$  molec  $\text{cm}^{-2}$  were observed in the  
 204 limb and zenith geometries, respectively.



205 **Figure 1.** Detection of IO radicals above Storm Peak Laboratory during April 2022. (a) IO  
 206 spectral proof for a “low IO” case on April 6 at 19:20:32 UTC corresponding to  $(0.6 \pm 0.1) \times 10^{13}$   
 207 molec  $\text{cm}^{-2}$  IO dSCD. (b) IO spectral proof for a “high IO” case on April 16 at 17:36:51 UTC  
 208 corresponding to  $(1.6 \pm 0.1) \times 10^{13}$  molec  $\text{cm}^{-2}$  IO dSCD. (c) Average STILT 24-hour back  
 209 trajectories for April 6 at 18:00 UTC and April 16 at 18:00 UTC.  
 210

211

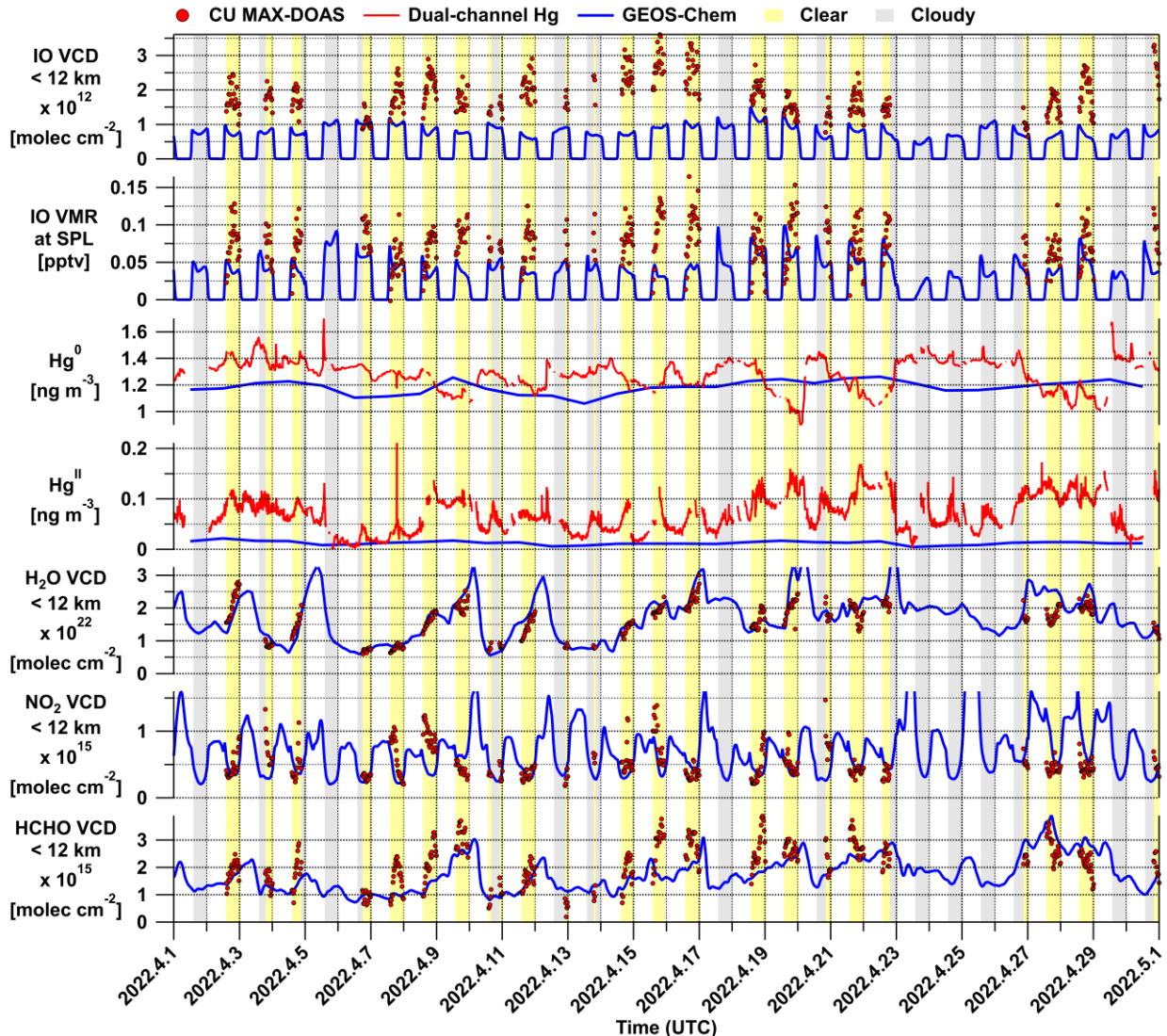
212

213 Sensitivity studies varying the a priori profile used for the IO column retrieval indicate  
214 that IO VMR increased with altitude. Two a priori profiles were tested: a “flat” profile with a  
215 constant 0.10 pptv IO throughout the atmosphere, and the GEOS-Chem April 2022 daytime  
216 average IO profile. The GEOS-Chem profile, in which IO VMR increases with altitude,  
217 consistently resulted in better agreement between measured and a posteriori simulated IO SCDs  
218 than the “flat” profile (Figure S2). Therefore, the GEOS-Chem profile was used in the IO  
219 retrieval as it is more physically representative of the measurements.

220 IO  $VCD_{trop}$  ( $VMR_{instr}$ ) was  $0.7\text{--}3.6 \times 10^{12}$  molec  $\text{cm}^{-2}$  (0.00–0.16 pptv), averaging  
221  $(1.9 \pm 0.6) \times 10^{12}$  molec  $\text{cm}^{-2}$  ( $0.08 \pm 0.03$  pptv). IO  $VCD_{trop}$  (IO  $VMR_{instr}$ ) error is  $0.5 \times 10^{12}$  molec  
222  $\text{cm}^{-2}$  (0.03 pptv), with contributions from choice of a priori settings ( $0.3 \times 10^{12}$  molec  $\text{cm}^{-2}$ ; 0.01  
223 pptv), uncertainty in  $SCD_{ref}$  ( $0.1 \times 10^{12}$  molec  $\text{cm}^{-2}$ ; <0.01 pptv), and method error (spectral  
224 fitting, radiative transfer modeling, optimal estimation;  $0.1 \times 10^{12}$  molec  $\text{cm}^{-2}$ ; 0.02 pptv).  
225 Uncertainty in the IO absorption cross section is 2%, and negligible (Spietz et al., 2005).

226 24-hour STILT back trajectories indicated that the observed air masses consistently  
227 originated from over the Pacific Ocean. The air mass observed during the day with the highest  
228 IO signal (April 16) originated from the southwest, towards the tropics (Figure 1c). The air mass  
229 observed during the day with the lowest IO signal (April 6) originated from the northwest,  
230 towards mid-latitudes. However, not all tropical air masses contained higher IO; on April 28, for  
231 example, the back-trajectories indicated an air mass originating even further south than on April  
232 16, yet the IO VCD was significantly larger on April 16 than on April 28. While air mass origin  
233 alone cannot account for the observed IO variability, we consistently found higher IO in air  
234 masses with less than 24-hour transport time from the Pacific Ocean. This indicated that IO  
235 variability also depended on the strength of IO sinks along the transport path, which are not  
236 constrained in our analysis.

237 IO  $VCD_{trop}$  and  $VMR_{instr}$  were up to three times larger, and the range of IO  $VCD_{trop}$  and  
238  $VMR_{instr}$  was larger than predicted by GEOS-Chem (Figure 2). GEOS-Chem daytime IO  $VCD_{trop}$   
239 ( $VMR_{instr}$ ) was  $0.3\text{--}1.5 \times 10^{12}$  molec  $\text{cm}^{-2}$  (0.0007–0.10 pptv), averaging  $0.8 \pm 0.2 \times 10^{12}$  molec  $\text{cm}^{-2}$   
240 ( $0.04 \pm 0.02$  pptv), two times smaller than observed. There was no correlation between measured  
241 and modeled IO  $VCD_{trop}$ . There was a very weak but statistically significant anti-correlation  
242 between measured and modeled IO  $VMR_{instr}$  ( $R: -0.20 \pm 0.05$ ;  $p < 1 \times 10^{-4}$ ). The two days with the  
243 lowest IO  $VCD_{trop}$ , April 6 and 26, showed reasonable agreement with GEOS-Chem. However,  
244 on all other days, IO  $VCD_{trop}$  was significantly larger than predicted. The GEOS-Chem  
245 horizontal grid cell size ( $0.5^\circ \times 0.625^\circ$ ) is comparable to the tens of kilometers sampled by the  
246 MAX-DOAS light path. The similar magnitude of underestimation of IO  $VCD_{trop}$  and  $VMR_{instr}$   
247 by GEOS-Chem provides evidence that IO VMR increased with altitude, since GEOS-Chem  
248 consistently simulated increasing IO VMR with altitude. One would expect the GEOS-Chem  
249 underestimation to be different between IO  $VCD_{trop}$  and  $VMR_{instr}$  if the measured profile shape  
250 was very different than modeled.



251

252 **Figure 2.** Measurements of IO,  $\text{Hg}^0$ ,  $\text{Hg}^{\text{II}}$ ,  $\text{H}_2\text{O}$ ,  $\text{NO}_2$ , and  $\text{HCHO}$  at Storm Peak Laboratory are  
253 compared with GEOS-Chem during April 2022.

### 254 3.2 Measurements of other gases at SPL

255 During April 1–30, 2022 at SPL, GEOS-Chem very accurately simulated both  $\text{H}_2\text{O}$   
256 magnitude and temporal variability; very accurately simulated  $\text{NO}_2$  magnitude but failed to  
257 simulate  $\text{NO}_2$  temporal variability; and accurately simulated  $\text{HCHO}$  magnitude but had only  
258 moderate success in simulating  $\text{HCHO}$  temporal variability.

#### 259 3.2.1 $\text{H}_2\text{O}$

260  $\text{H}_2\text{O}$  VCD<sub>trop</sub> ( $\text{VMR}_{\text{instr}}$ ) was  $0.6\text{--}3.0 \times 10^{22}$  molec  $\text{cm}^{-2}$  (0.4–2.8‰), averaging  
261  $1.6 \pm 0.5 \times 10^{22}$  molec  $\text{cm}^{-2}$  ( $1.5 \pm 0.5$  ‰). Total error for  $\text{H}_2\text{O}$  VCD<sub>trop</sub> ( $\text{VMR}_{\text{instr}}$ ) is  $0.2 \times 10^{22}$  molec  
262  $\text{cm}^{-2}$  (0.1‰). There was no correlation between  $\text{H}_2\text{O}$  VCD<sub>trop</sub> and IO VCD<sub>trop</sub>, and a weak  
263 correlation between  $\text{H}_2\text{O}$  VMR<sub>instr</sub> and IO VMR<sub>instr</sub> ( $R: 0.35 \pm 0.05$ ;  $p < 1 \times 10^{-5}$ ).

264 GEOS-Chem daytime H<sub>2</sub>O VCD<sub>trop</sub> (VMR<sub>instr</sub>) is from the MERRA-2 reanalysis and was  
 265 0.6–3.8×10<sup>22</sup> molec cm<sup>-2</sup> (0.7–6.8‰), averaging 1.7±0.7×10<sup>22</sup> molec cm<sup>-2</sup> (3.1±1.2 ‰). The  
 266 measured and modeled H<sub>2</sub>O VCD<sub>trop</sub> variations were strongly correlated ( $R: 0.76\pm0.03$ ;  $p<1\times10^{-5}$ )  
 267 and agreed well (Figure 2), indicating model skill in simulating atmospheric H<sub>2</sub>O column  
 268 variability due to passing frontal systems, consistent with earlier observations (Bosilovich et al.  
 269 2017). This agreement corroborates control over radiative transfer in the column retrieval  
 270 method that applies to all trace gas columns presented here.

### 271 3.2.2 NO<sub>2</sub>

272 NO<sub>2</sub> VCD<sub>trop</sub> (VMR<sub>instr</sub>) was 0.2–1.5×10<sup>15</sup> molec cm<sup>-2</sup> (0.01–0.26 ppbv), averaging  
 273 0.5±0.2×10<sup>15</sup> molec cm<sup>-2</sup> (0.08±0.05 ppbv). Total error for NO<sub>2</sub> VCD<sub>trop</sub> (VMR<sub>instr</sub>) is 0.4×10<sup>15</sup>  
 274 molec cm<sup>-2</sup> (0.01 ppbv). There was no correlation between the NO<sub>2</sub> VCD<sub>trop</sub> and IO VCD<sub>trop</sub> or  
 275 between NO<sub>2</sub> VMR<sub>instr</sub> and IO VMR<sub>instr</sub>, which is expected due to different sources.

276 GEOS-Chem daytime NO<sub>2</sub> VCD<sub>trop</sub> (VMR<sub>instr</sub>) was 0.2–1.6×10<sup>15</sup> molec cm<sup>-2</sup> (0.01–0.24  
 277 ppbv), averaging 0.5±0.2×10<sup>15</sup> molec cm<sup>-2</sup> (0.07±0.03 ppbv). GEOS-Chem struggled to  
 278 accurately simulate tropospheric NO<sub>2</sub> at SPL; this is consistent with previously observed model-  
 279 measurement disagreement in tropospheric NO<sub>2</sub> (Shah et al., 2023). While the range and average  
 280 for the columns and concentrations closely agree with those observed, there was no correlation  
 281 between measured and modeled NO<sub>2</sub> VCD<sub>trop</sub> or VMR<sub>instr</sub>.

### 282 3.2.3 HCHO

283 HCHO VCD<sub>trop</sub> (VMR<sub>instr</sub>) was 0.2–3.9×10<sup>15</sup> molec cm<sup>-2</sup> (-0.02–0.67 ppbv), averaging  
 284 2.2±0.8×10<sup>15</sup> molec cm<sup>-2</sup> (0.36±0.15 ppbv). Total error for HCHO VCD<sub>trop</sub> (VMR<sub>instr</sub>) is 0.2×10<sup>15</sup>  
 285 molec cm<sup>-2</sup> (0.03 ppbv). There was no correlation between HCHO VCD<sub>trop</sub> and IO VCD<sub>trop</sub>, and  
 286 a weak correlation between HCHO VMR<sub>instr</sub> and IO VMR<sub>instr</sub> ( $R: 0.31\pm0.05$ ;  $p<1\times10^{-5}$ ).

287 GEOS-Chem daytime HCHO VCD<sub>trop</sub> (VMR<sub>instr</sub>) was 0.7–3.9×10<sup>15</sup> molec cm<sup>-2</sup> (0.0–0.7  
 288 ppbv), averaging 1.7±0.6×10<sup>15</sup> molec cm<sup>-2</sup> (0.3±0.1 ppbv). The observed HCHO was  
 289 systematically higher than predicted. The correlation between measured and modeled HCHO  
 290 VCD<sub>trop</sub> was moderate ( $R: 0.57\pm0.04$ ;  $p<1\times10^{-5}$ ), and a strong correlation was found between  
 291 measured and modeled HCHO VMR<sub>instr</sub> ( $R: 0.66\pm0.04$ ;  $p<1\times10^{-5}$ ). Overall, the range and  
 292 average for HCHO VCD<sub>trop</sub> and VMR<sub>instr</sub> agree closely with those observed, and the model had  
 293 better skill in predicting HCHO variability than NO<sub>2</sub> or IO variability at SPL.

### 294 3.2.4 BrO

295 A measurement constraint on bromine was not possible during the study period. The  
 296 amount of tropospheric BrO observed at SPL was consistently below the detection limit of ~0.5  
 297 pptv VMR<sub>instr</sub>. The GEOS-Chem April 2022 daytime average BrO VMR<sub>instr</sub> at SPL was 0.15  
 298 pptv, consistent with the observations and too low to be observable even with the state-of-the-art  
 299 MAX-DOAS instrument used here. We therefore used the GEOS-Chem BrO profile without  
 300 modifications to constrain the mercury box model.

### 301 3.3 Mercury

302 Hg<sup>0</sup><sub>(g)</sub> (Hg<sup>II</sup>) was 0.90–1.70 ng m<sup>-3</sup> (0–211 pg m<sup>-3</sup>), averaging 1.28±0.11 ng m<sup>-3</sup> (68±34  
 303 pg m<sup>-3</sup>). Interestingly, there was a weak anti-correlation between Hg<sup>0</sup><sub>(g)</sub> and HCHO VMR<sub>instr</sub> ( $R:$   
 304  $-0.35\pm0.05$ ;  $p<1\times10^{-5}$ ), and a moderately strong correlation between Hg<sup>II</sup> and HCHO VMR<sub>instr</sub>

305 (R:  $0.64 \pm 0.04$ ;  $p < 1 \times 10^{-5}$ ), indicating a possible connection between mercury oxidation and total  
306 atmospheric oxidative capacity.

307 Oxidized mercury at SPL coincided with warm air masses at low relative humidity,  
308 consistent with past work (Fain et al., 2009), but also at high absolute humidity. There was a  
309 weak anti-correlation between  $\text{Hg}_{(g)}^0$  and measured temperature (R:  $-0.37 \pm 0.02$ ;  $p < 1 \times 10^{-5}$ ), a  
310 strong correlation between  $\text{Hg}^{\text{II}}$  and measured temperature (R:  $0.70 \pm 0.01$ ;  $p < 1 \times 10^{-5}$ ), a weak  
311 correlation between  $\text{Hg}_{(g)}^0$  and measured relative humidity (R:  $0.39 \pm 0.02$ ;  $p < 1 \times 10^{-5}$ ), a moderate  
312 anti-correlation between  $\text{Hg}^{\text{II}}$  and measured relative humidity (R:  $-0.43 \pm 0.01$ ;  $p < 1 \times 10^{-5}$ ), and a  
313 weak correlation between  $\text{Hg}^{\text{II}}$  and  $\text{H}_2\text{O}$  VMR<sub>instr</sub> (R:  $0.37 \pm 0.04$ ;  $p < 1 \times 10^{-5}$ ). This is consistent  
314 with the idea that mercury survives longer in air masses with less wet deposition, providing more  
315 time for oxidation to occur.

316 GEOS-Chem  $\text{Hg}_{(g)}^0$  ( $\text{Hg}^{\text{II}}$ ) was  $1.06\text{--}1.26 \text{ ng m}^{-3}$  ( $4\text{--}22 \text{ pg m}^{-3}$ ), averaging  $1.18 \pm 0.05 \text{ ng}$   
317  $\text{m}^{-3}$  ( $12 \pm 4 \text{ pg m}^{-3}$ ). While measured and modeled  $\text{Hg}^0$  concentrations agreed reasonably well,  
318 there was no correlation in  $\text{Hg}^0$  temporal variability. Moreover, the measured  $\text{Hg}^{\text{II}}$  concentration  
319 was up to ten times larger and more variable (i.e., a six times larger standard deviation) than  
320 modeled (Figure 2). Despite these differences, measured and modeled  $\text{Hg}^{\text{II}}$  were moderately  
321 correlated (R:  $0.47 \pm 0.01$ ;  $p < 1 \times 10^{-5}$ ), indicating that GEOS-Chem had some skill in predicting  
322  $\text{Hg}^{\text{II}}$  variability at SPL but not the magnitude. Increased  $\text{Hg}^{\text{II}}$  sources (i.e., iodine-induced  
323 oxidation) and/or decreased  $\text{Hg}^{\text{II}}$  sinks in the model are needed to explain this model-  
324 measurement disagreement.

## 325 4 Discussion

### 326 4.1 Literature comparison

327 The observed IO VCD<sub>trop</sub> monthly average of  $1.9 \pm 0.6 \times 10^{12} \text{ molec cm}^{-2}$  over the central  
328 continental U.S. is consistent with the few previous airborne measurements. Dix et al. (2013)  
329 reported an IO VCD<sub>trop</sub> of  $2.49$  to  $2.91 \times 10^{12} \text{ molec cm}^{-2}$  over the central Pacific and Volkamer et  
330 al. (2015) found  $2.1$  to  $2.5 \times 10^{12} \text{ molec cm}^{-2}$  over the eastern Pacific; both studies probed tropical  
331 air in the northern hemisphere winter. The average IO VCD<sub>trop</sub> above SPL demonstrates that  
332 iodine is widespread in the free troposphere, including over continents.

333 The significant day-to-day temporal variability in IO VCD<sub>trop</sub> over the central continental  
334 U.S. ( $0.7 \pm 0.5$  to  $3.6 \pm 0.5 \times 10^{12} \text{ molec cm}^{-2}$ ) has not been previously observed. Our measurements  
335 also characterize IO VCD<sub>trop</sub> for the first time in the spring. Information about iodine  
336 spatiotemporal variability in the free troposphere is extremely scarce. Two sources affecting free  
337 tropospheric IO variability are marine convection (Dix et al., 2013) and dust (Puente et al.,  
338 2012; Koenig et al., 2021). Regional-scale IO variability over the Eastern Pacific Ocean was  
339 systematically probed by Wang et al. (2015), who reported IO VCD<sub>trop</sub> of  $2.6$  to  $3.5 \times 10^{12} \text{ molec}$   
340  $\text{cm}^{-2}$  and  $5.1 \times 10^{12} \text{ molec cm}^{-2}$  in the southern hemisphere tropical and subtropical Pacific,  
341 respectively, during Austral summer. Some of this variability could be attributed to dust sources  
342 of iodine from the Sechura and Atacama deserts (Koenig et al., 2021), with regional impacts on  
343 ozone in the marine boundary layer and free troposphere. Puente et al. (2012) reported  
344 variability in IO dSCDs related to Saharan dust impacts in the free troposphere over Tenerife  
345 Island in the Eastern Atlantic; they did not attempt to retrieve IO VCD<sub>trop</sub>. Elevated IO VCD<sub>trop</sub>  
346 over SPL is related to rapid transport from the Pacific Ocean, consistent with marine convection  
347 upwind, and unrelated to immediate dust impacts.

348 Schönhardt et al. (2008) reported global satellite measurements of IO SCDs. Their  
 349 analysis used a reference spectrum over the tropical Pacific, where airborne measurements  
 350 indicate that there is a significant IO VCD<sub>trop</sub> (Dix et al., 2013; Volkamer et al., 2015). Therefore,  
 351 the satellite IO SCDs are lower limits and not directly comparable to our measurements.

### 352 4.2 Ozone relevance

353 Iodine is responsible for a ~9% reduction in the total tropospheric ozone burden, and  
 354 model-measurement agreement for IO profiles over the eastern tropical Pacific indicates that  
 355 marine sources for IO are reasonably well-constrained (Wang et al., 2021). The consistent low  
 356 bias in modeled IO compared to our observations suggests that iodine's contribution to  
 357 tropospheric ozone destruction may be higher than currently estimated over continents. In  
 358 particular, GEOS-Chem iodine chemistry has not been significantly updated since version 11-02-  
 359 rc, with the implementation of Wang et al. (2021) in version 12.9 leaving the mechanism of  
 360 Sherwen et al. (2016b) largely unchanged.

### 361 4.3 Implications for atmospheric mercury oxidation

362 Iodine oxidation of mercury is deemed unimportant, and is therefore missing in  
 363 atmospheric models, in part due to the lower Hg-I bond strength (8.3–10.9 kcal mol<sup>-1</sup>) compared  
 364 to Hg-Br (14.4–17.9 kcal mol<sup>-1</sup>) and Hg-OH (9.4–12.4 kcal mol<sup>-1</sup>) (Goodsite et al., 2004; Shepler  
 365 et al., 2005; Cremer et al., 2008; Dibble et al., 2020). The Hg-OH bond strength was previously  
 366 thought to be too weak to lead to Hg<sup>II</sup> formation, but the discovery that the reaction of Hg<sup>I</sup>  
 367 species with ozone is kinetically barrierless (Saiz-Lopez et al., 2020) has resulted in a re-  
 368 evaluation of the global relevance of OH radicals to Hg<sup>0(g)</sup> oxidation (Shah et al., 2021; Castro et  
 369 al., 2022; Hewa Edirappulige et al., 2023). There is evidence suggesting that the reaction of  
 370 Hg<sup>0(g)</sup> with I atom proceeds faster than with Br atom (Goodsite et al., 2004). In light of the larger  
 371 than predicted amounts of tropospheric iodine over continents, the Hg-I bond strength and  
 372 Hg<sup>I(I)<sub>(g)</sub></sup> dissociation rate warrant re-evaluation.

373 Our box model results (Figure 3) show that I atoms may oxidize Hg<sup>0</sup> at rates rivaling Br  
 374 atoms at cold temperatures typical of the free troposphere (4–12 km; <260K). Above 9 km, this  
 375 finding is independent of the assumed Hg-I bond strength, as Hg<sup>I(I)<sub>(g)</sub></sup> dissociation is slow at cold  
 376 temperatures. Below 9 km, iodine-induced Hg oxidation may rival Br depending on the assumed  
 377 Hg-I bond strength, which is highly uncertain. Our most conservative estimate, which uses the  
 378 Hg+Br kinetics measured by Donohoue et al. (2006) for the Hg+I reaction and assumes that  
 379 Hg<sup>I(I)</sup> dissociates 100 times faster than Hg<sup>I(OH)</sup>, places iodine atoms at a contribution of 1.2%–  
 380 42.1% to Hg<sup>II(g)</sup> formation below 12 km (Br: 17.4–68.3%; OH: 7.6–81.1%; Cl: <0.5%). Our least  
 381 conservative estimate, which uses the bimolecular rate constant calculated by Goodsite et al.  
 382 (2004) for the Hg+I reaction and assumes that Hg<sup>I(I)</sup> dissociates at the same rate as Hg<sup>I(OH)</sup>,  
 383 places iodine atoms at a contribution of 40.1–78.7% to Hg<sup>II(g)</sup> formation below 12 km (Br: 12.4–  
 384 46.9%; OH: 6.4–57.8%; Cl: <0.5%). These results are consistent with the observed correlation  
 385 between mercury and iodine in aerosols in the lower stratosphere (Murphy et al., 2006), and  
 386 suggest these correlations might have a mechanistic causal relationship. The inclusion of iodine  
 387 radical oxidation of Hg<sup>0(g)</sup> to Hg<sup>II</sup> in atmospheric models is desirable and will benefit from better  
 388 knowledge of the chemical kinetics, from laboratory experiments and calculations, and better  
 389 constraints on the tropospheric iodine distribution.

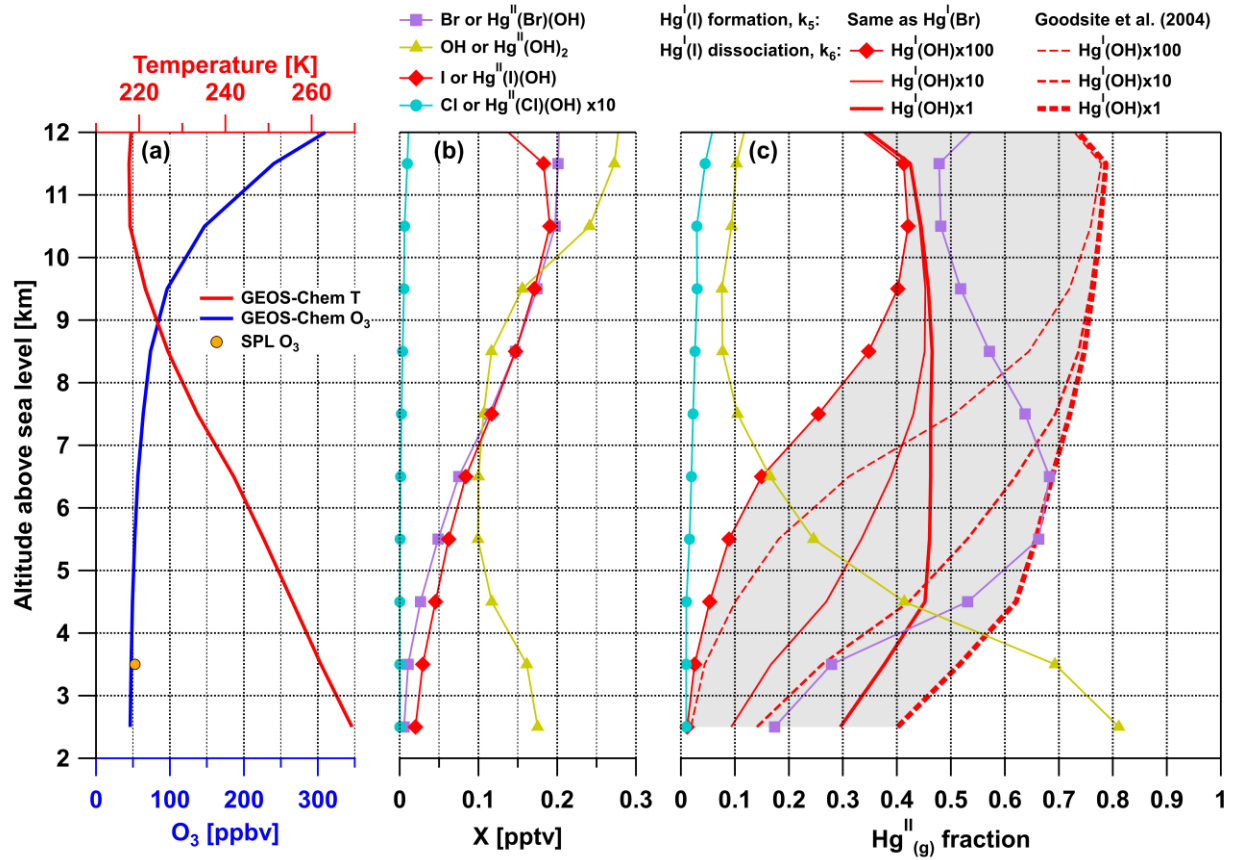


**Figure 3.** Iodine-initiated  $\text{Hg}^0$  oxidation compared with other radical pathways above Storm Peak Laboratory. Iodine appears to be a competitive oxidant throughout the troposphere and becomes more relevant at colder temperatures in the upper free troposphere. See Section 2.2.3, Section 4.3, Text S3, Table S5, and Table S6 for details.

## Acknowledgments

Funding from the U.S. National Science Foundation (AGS-1951513, AGS-1951514, AGS-1951515, AGS-1951632) is gratefully acknowledged. The Steamboat Ski Resort, Maria Garcia, Dan Gilchrist, and SPL staff provided logistical support. Caroline Womack and Jessica Haskins assisted with F0AM. The Global Modeling and Assimilation Office at NASA Goddard Space Flight Center provided MERRA-2 meteorological data.

## Data availability statement

All CU MAX-DOAS and dual-channel mercury system measurement data at Storm Peak Laboratory during April 2022 (measured and GEOS-Chem simulated trace gas SCD,  $\text{VCD}_{\text{trop}}$ ,

404 VMR<sub>instr</sub>; measured and GEOS-Chem simulated Hg<sup>0</sup> & Hg<sup>II</sup>) as well as the gas-phase mercury  
405 chemical box model constraints & output described in this study are publicly available at zenodo  
406 via <https://zenodo.org/doi/10.5281/zenodo.10805549> with a Creative Commons Attribution 4.0  
407 license. The HYSPLIT-STILT back trajectory simulations at Storm Peak Laboratory during  
408 April 2022 described in this study are publicly available at zenodo via  
409 <https://doi.org/10.5281/zenodo.10806478> with a Creative Commons Attribution 4.0 license. The  
410 long-term measurements of Hg<sup>0</sup>, Hg<sup>II</sup>, trace gases, and meteorology at Storm Peak Laboratory, a  
411 subset of which are used in this study, are publicly available at zenodo via  
412 <https://doi.org/10.5281/zenodo.10699270> with a Creative Commons Attribution 4.0 license.  
413 Version 13.2.1 of the GEOS-Chem model was used to simulate atmospheric oxidant fields, is  
414 preserved at <https://doi.org/10.5281/zenodo.5500717>, is available via an MIT license, and is  
415 developed openly at <https://github.com/geoschem/GCClassic/tree/13.2.1>. Version 12.8.0 of the  
416 GEOS-Chem model was used to simulate atmospheric mercury chemistry, is preserved at  
417 <https://doi.org/10.5281/zenodo.3784796>, is available via an MIT license, and is developed  
418 openly at <https://github.com/geoschem/geos-chem/tree/12.8.0>. Version 3.4.5 of the QDOAS  
419 spectral analysis software developed by the DOAS UV-VIS team at the Royal Belgian Institute  
420 for Space Aeronomy (BIRA-IASB) was used for all DOAS spectral analysis, is available via a  
421 BSD 3-clause type license, and is developed openly at [https://github.com/UVVIS-BIRA-  
IASB/qdoas](https://github.com/UVVIS-BIRA-IASB/qdoas). Version 8.0.4.2 of the IGOR Pro software developed by WaveMetrics, Inc. was  
422 used for data analysis and is available via a commercial license at  
423 <https://www.wavemetrics.com/products/igorpro>. Vector map data of coastlines and state borders  
424 used in Panel (c) of Figure 1 are available at Natural Earth via <https://www.naturalearthdata.com/>  
425 with a public domain license.

427 **References**

- 428 Aliche, B., Hebestreit, K., Stutz, J., & Platt, U. (1999). Iodine oxide in the marine boundary  
429 layer. *Nature*, 397(6720), 572–573. <https://doi.org/10.1038/17508>
- 430 Allan, B. J., McFiggans, G., Plane, J. M. C., & Coe, H. (2000). Observations of iodine monoxide  
431 in the remote marine boundary layer. *Journal of Geophysical Research: Atmospheres*,  
432 105(D11), 14363–14369. <https://doi.org/10.1029/1999JD901188>
- 433 Baccarini, A., Karlsson, L., Dommen, J., Duplessis, P., Vüllers, J., Brooks, I. M., Saiz-Lopez, A.,  
434 Salter, M., Tjernström, M., Baltensperger, U., Zieger, P., & Schmale, J. (2020). Frequent  
435 new particle formation over the high Arctic pack ice by enhanced iodine emissions.  
436 *Nature Communications*, 11(1), 4924. <https://doi.org/10.1038/s41467-020-18551-0>
- 437 Bell, N., Hsu, L., Jacob, D. J., Schultz, M. G., Blake, D. R., Butler, J. H., King, D. B., Lobert, J.  
438 M., & Maier-Reimer, E. (2002). Methyl iodide: Atmospheric budget and use as a tracer  
439 of marine convection in global models. *Journal of Geophysical Research: Atmospheres*,  
440 107(D17), 4340. <https://doi.org/10.1029/2001JD001151>
- 441 Borys, R. D., & Wetzel, M. A. (1997). Storm Peak Laboratory: A Research, Teaching, and  
442 Service Facility for the Atmospheric Sciences. *Bulletin of the American Meteorological  
443 Society*, 78(10), 2115–2123. [https://doi.org/10.1175/1520-0477\(1997\)078%3C2115:SPLART%3E2.0.CO;2](https://doi.org/10.1175/1520-0477(1997)078%3C2115:SPLART%3E2.0.CO;2)
- 445 Bosilovich, M. G., Robertson, F. R., Takacs, L., Molod, A., & Mocko, D. (2017). Atmospheric  
446 Water Balance and Variability in the MERRA-2 Reanalysis. *Journal of Climate*, 30(4),  
447 1177–1196. <https://doi.org/10.1175/JCLI-D-16-0338.1>
- 448 Carpenter, L. J., MacDonald, S. M., Shaw, M. D., Kumar, R., Saunders, R. W., Parthipan, R.,  
449 Wilson, J., & Plane, J. M. C. (2013). Atmospheric iodine levels influenced by sea surface

- 450        emissions of inorganic iodine. *Nature Geoscience*, 6(2), 108–111.
- 451        <https://doi.org/10.1038/ngeo1687>
- 452        Castro, P. J., Kellö, V., Cernušák, I., & Dibble, T. S. (2022). Together, Not Separately, OH and
- 453        O<sub>3</sub> Oxidize Hg<sup>(0)</sup> to Hg<sup>(II)</sup> in the Atmosphere. *The Journal of Physical Chemistry A*,
- 454        126(44), 8266–8279. <https://doi.org/10.1021/acs.jpca.2c04364>
- 455        Coburn, S., Dix, B., Edgerton, E., Holmes, C. D., Kinnison, D., Liang, Q., ter Schure, A., Wang,
- 456        S., & Volkamer, R. (2016). Mercury oxidation from bromine chemistry in the free
- 457        troposphere over the southeastern US. *Atmospheric Chemistry and Physics*, 16(6), 3743–
- 458        3760. <https://doi.org/10.5194/acp-16-3743-2016>
- 459        Coburn, S., Dix, B., Sinreich, R., & Volkamer, R. (2011). The CU ground MAX-DOAS
- 460        instrument: characterization of RMS noise limitations and first measurements near
- 461        Pensacola, FL of BrO, IO, and CHOCHO. *Atmospheric Measurement Techniques*, 4(11),
- 462        2421–2439. <https://doi.org/10.5194/amt-4-2421-2011>
- 463        Cremer, D., Kraka, E., & Filatov, M. (2008). Bonding in Mercury Molecules Described by the
- 464        Normalized Elimination of the Small Component and Coupled Cluster Theory.
- 465        *ChemPhysChem*, 9(17), 2510–2521. <https://doi.org/10.1002/cphc.200800510>
- 466        Cuevas, C. A., Maffezzoli, N., Corella, J. P., Spolaor, A., Valletlonga, P., Kjær, H. A., Simonsen,
- 467        M., Winstrup, M., Vinther, B., Horvat, C., Fernandez, R. P., Kinnison, D., Lamarque, J.-
- 468        F., Barbante, C., & Saiz-Lopez, A. (2018). Rapid increase in atmospheric iodine levels in
- 469        the North Atlantic since the mid-20th century. *Nature Communications*, 9(1), 1452.
- 470        <https://doi.org/10.1038/s41467-018-03756-1>
- 471        Deutschmann, T., Beirle, S., Frieß, U., Grzegorski, M., Kern, C., Kritten, L., Platt, U., Prados-
- 472        Román, C., Pukīte, J., Wagner, T., Werner, B., & Pfeilsticker, K. (2011). The Monte

- 473 Carlo atmospheric radiative transfer model McArtim: Introduction and validation of  
474 Jacobians and 3D features. *Journal of Quantitative Spectroscopy and Radiative Transfer*,  
475 112(6), 1119–1137. <https://doi.org/10.1016/j.jqsrt.2010.12.009>
- 476 Dibble, T. S., Tetu, H. L., Jiao, Y., Thackray, C. P., & Jacob, D. J. (2020). Modeling the OH-  
477 Initiated Oxidation of Mercury in the Global Atmosphere without Violating Physical  
478 Laws. *The Journal of Physical Chemistry A*, 124(2), 444–453.  
479 <https://doi.org/10.1021/acs.jpca.9b10121>
- 480 Dix, B., Baidar, S., Bresch, J. F., Hall, S. R., Schmidt, K. S., Wang, S., & Volkamer, R. (2013).  
481 Detection of iodine monoxide in the tropical free troposphere. *Proceedings of the  
482 National Academy of Sciences*, 110(6), 2035–2040.  
483 <https://doi.org/10.1073/pnas.1212386110>
- 484 Donohoue, D. L., Bauer, D., Cossairt, B., & Hynes, A. J. (2006). Temperature and Pressure  
485 Dependent Rate Coefficients for the Reaction of Hg with Br and the Reaction of Br with  
486 Br: A Pulsed Laser Photolysis-Pulsed Laser Induced Fluorescence Study. *The Journal of  
487 Physical Chemistry A*, 110(21), 6623–6632. <https://doi.org/10.1021/jp054688j>
- 488 Elgiar, T. R., Lyman, S. N., O’Neil, T., Gratz, L. E., Nair, S. V., Živković, I., Horvat, M.,  
489 Andron, T. D., & Hallar, G. (in preparation). NIST-Traceable Calibration of Atmospheric  
490 Oxidized Mercury Measurements.
- 491 Faïn, X., Obrist, D., Hallar, A. G., McCubbin, I., & Rahn, T. (2009). High levels of reactive  
492 gaseous mercury observed at a high elevation research laboratory in the Rocky  
493 Mountains. *Atmospheric Chemistry and Physics*, 9(20), 8049–8060.  
494 <https://doi.org/10.5194/acp-9-8049-2009>

- 495 Gratz, L. E., Lyman, S. N., Elgiar, T., Hallar, A. G., & Volkamer, R. (2024). Measurements of  
496 atmospheric mercury, trace gases, aerosols, and meteorology at Storm Peak Laboratory,  
497 Colorado, in 2021 and 2022 (version 1) [Dataset]. Zenodo.  
498 <https://doi.org/10.5281/zenodo.10699270>
- 499 Finkenzeller, H., Iyer, S., He, X.-C., Simon, M., Koenig, T. K., Lee, C. F., Valiev, R., Hofbauer,  
500 V., Amorim, A., Baalbaki, R., Baccarini, A., Beck, L., Bell, D. M., Caudillo, L., Chen,  
501 D., Chiu, R., Chu, B., Dada, L., Duplissy, J., Heinritzi, M., Kemppainen, D., Kim, C.,  
502 Krechmer, J., Kürten, A., Kvashnin, A., Lamkaddam, H., Lee, C. P., Lehtipalo, K., Li, Z.,  
503 Makhmutov, V., Manninen, H. E., Marie, G., Marten, R., Mauldin, R. L., Mentler, B.,  
504 Müller, T., Petäjä, T., Philippov, M., Ranjithkumar, A., Rörup, B., Shen, J., Stolzenburg,  
505 D., Tauber, C., Tham, Y. J., Tomé, A., Vazquez-Pufleau, M., Wagner, A. C., Wang, D.  
506 S., Wang, M., Wang, Y., Weber, S. K., Nie, W., Wu, Y., Xiao, M., Ye, Q., Zauner-  
507 Wieczorek, M., Hansel, A., Baltensperger, U., Brioude, J., Curtius, J., Donahue, N. M.,  
508 El Haddad, I., Flagan, R. C., Kulmala, M., Kirkby, J., Sipilä, M., Worsnop, D. R., Kurten,  
509 T., Rissanen, M. & Volkamer, R. (2023). The gas-phase formation mechanism of iodic  
510 acid as an atmospheric aerosol source. *Nature Chemistry*, 15(1), 129–135.  
511 <https://doi.org/10.1038/s41557-022-01067-z>
- 512 Friess, U., Deutschmann, T., Gilfedder, B. S., Weller, R., & Platt, U. (2010). Iodine monoxide in  
513 the Antarctic snowpack. *Atmospheric Chemistry and Physics*, 10(5), 2439–2456.  
514 <https://doi.org/10.5194/acp-10-2439-2010>
- 515 Furneaux, K. L., Whalley, L. K., Heard, D. E., Atkinson, H. M., Bloss, W. J., Flynn, M. J.,  
516 Gallagher, M. W., Ingham, T., Kramer, L., Lee, J. D., Leigh, R., McFiggans, G. B.,  
517 Mahajan, A. S., Monks, P. S., Oetjen, H., Plane, J. M. C., & Whitehead, J. D. (2010).

- 518 Measurements of iodine monoxide at a semi polluted coastal location. *Atmospheric*  
519 *Chemistry and Physics*, 10(8), 3645–3663. <https://doi.org/10.5194/acp-10-3645-2010>
- 520 Gielen, C., van Roozendael, M., Hendrick, F., Pinardi, G., Vlemmix, T., de Bock, V., de Backer,  
521 H., Fayt, C., Hermans, C., Gillotay, D., & Wang, P. (2014). A simple and versatile cloud-  
522 screening method for MAX-DOAS retrievals. *Atmospheric Measurement Techniques*,  
523 7(10), 3509–3527. <https://doi.org/10.5194/amt-7-3509-2014>
- 524 Goddard Earth Observing System (GEOS) global 3-D model of atmospheric chemistry.  
525 geoschem/GCClassic: GEOS-Chem 12.8.0 [Software]. Zenodo.  
526 <https://doi.org/10.5281/zenodo.3784796>
- 527 Goddard Earth Observing System (GEOS) global 3-D model of atmospheric chemistry.  
528 geoschem/GCClassic: GEOS-Chem 13.2.1 [Software]. Zenodo.  
529 <https://doi.org/10.5281/zenodo.5500717>
- 530 Gómez Martín, J. C., Lewis, T. R., James, A. D., Saiz-Lopez, A., & Plane, J. M. C. (2022).  
531 Insights into the Chemistry of Iodine New Particle Formation: The Role of Iodine Oxides  
532 and the Source of Iodic Acid. *Journal of the American Chemical Society*, 144(21), 9240–  
533 9253. <https://doi.org/10.1021/jacs.1c12957>
- 534 Gómez Martín, J. C., Mahajan, A. S., Hay, T. D., Prados-Román, C., Ordóñez, C., MacDonald,  
535 S. M., Plane, J. M. C., Sorribas, M., Gil, M., Paredes Mora, J. F., Agama Reyes, M. v.,  
536 Oram, D. E., Leedham, E., & Saiz-Lopez, A. (2013). Iodine chemistry in the eastern  
537 Pacific marine boundary layer. *Journal of Geophysical Research: Atmospheres*, 118(2),  
538 887–904. <https://doi.org/10.1002/jgrd.50132>
- 539 Großmann, K., Friess, U., Peters, E., Wittrock, F., Lampel, J., Yilmaz, S., Tscharitter, J.,  
540 Sommariva, R., von Glasow, R., Quack, B., Krüger, K., Pfeilsticker, K., & Platt, U.

- 541 (2013). Iodine monoxide in the Western Pacific marine boundary layer. *Atmospheric*  
542 *Chemistry and Physics*, 13(6), 3363–3378. <https://doi.org/10.5194/acp-13-3363-2013>
- 543 Goodsite, M. E., Plane, J. M. C., & Skov, H. (2004). A Theoretical Study of the Oxidation of  
544  $\text{Hg}^0$  to  $\text{HgBr}_2$  in the Troposphere. *Environmental Science & Technology*, 38(6), 1772–  
545 1776. <https://doi.org/10.1021/es034680s>
- 546 Hallar, A. G., Petersen, R., McCubbin, I. B., Lowenthal, D., Lee, S., Andrews, E., & Yu, F.  
547 (2016). Climatology of New Particle Formation and Corresponding Precursors at Storm  
548 Peak Laboratory. *Aerosol and Air Quality Research*, 16(3), 816–826.  
549 <https://doi.org/10.4209/aaqr.2015.05.0341>
- 550 Hendrick, F., van Roozendael, M., Chipperfield, M. P., Dorf, M., Goutail, F., Yang, X., Fayt, C.,  
551 Hermans, C., Pfeilsticker, K., Pommereau, J.-P., Pyle, J. A., Theys, N., & de Mazière, M.  
552 (2007). Retrieval of stratospheric and tropospheric BrO profiles and columns using  
553 ground-based zenith-sky DOAS observations at Harestua, 60° N. *Atmospheric Chemistry*  
554 and Physics, 7(18), 4869–4885. <https://doi.org/10.5194/acp-7-4869-2007>
- 555 Hewa Edirappulige, D. T., Kirby, I. J., Beckett, C. K., & Dibble, T. S. (2023). Atmospheric  
556 Chemistry of  $\text{HOHg}^{(\text{II})}\text{O}^\cdot$  Mimics That of a Hydroxyl Radical. *The Journal of Physical*  
557 *Chemistry A*, 127(40), 8392–8403. <https://doi.org/10.1021/acs.jpca.3c04159>
- 558 He, X.-C., Tham, Y. J., Dada, L., Wang, M., Finkenzeller, H., Stolzenburg, D., Iyer, S., Simon,  
559 M., Kürten, A., Shen, J., Rörup, B., Rissanen, M., Schobesberger, S., Baalbaki, R., Wang,  
560 D. S., Koenig, T. K., Jokinen, T., Sarnela, N., Beck, L. J., Almeida, J., Amanatidis, S.,  
561 Amorim, A., Ataei, F., Baccarini, A., Bertozzi, B., Bianchi, F., Brilke, S., Caudillo, L.,  
562 Chen, D., Chiu, R., Chu, B., Dias, A., Ding, A., Dommen, J., Duplissy, J., El Haddad, I.,  
563 Gonzalez Carracedo, L., Granzin, M., Hansel, A., Heinritzi, M., Hofbauer, V., Junninen,

- 564 H., Kangasluoma, J., Kemppainen, D., Kim, C., Kong, W., Krechmer J. E., Kvashin, A.,  
565 Laitinen, T., Lamkaddam, H., Lee, C. P., Lehtipalo, K., Leiminger, M., Li, Z.,  
566 Makhmutov, V., Manninen, H. E., Marie, G., Marten, R., Mathot, S., Mauldin, R. L.,  
567 Mentler, B., Möhler, O., Müller, T., Nie, W., Onnela, A., Petäjä, T., Pfeifer, J., Philippov,  
568 M., Ranjithkumar, A., Saiz-Lopez, A., Salma, I., Scholz, W., Schuchmann, S., Schulze,  
569 B., Steiner, G., Stozhkov, Y., Tauber, C., Tomé, A., Thakur, R. C., Väisänen, O.,  
570 Vazquez-Pufleau, M., Wagner, A. C., Wang, Y., Weber, S. K., Winkler, P. M., Wu, Y.,  
571 Xiao, M., Yan, C., Ye, Q., Ylisirniö, A., Zauner-Wieczorek, M., Zha, Q., Zhou, P.,  
572 Flagan, R. C., Curtius, J., Baltensperger, U., Kulmala, M., Kerminen, V.-M., Kurtén, T.,  
573 Donahue, N. M., Volkamer, R., Kirkby, J., Worsnop, D. R., Sipilä, M. (2021). Role of  
574 iodine oxoacids in atmospheric aerosol nucleation. *Science*, 371(6529), 589–595.  
575 <https://doi.org/10.1126/science.abe0298>
- 576 Inamdar, S., Tinel, L., Chance, R., Carpenter, L. J., Sabu, P., Chacko, R., Tripathy, S. C., Kerkar,  
577 A. U., Sinha, A. K., Bhaskar, P. V., Sarkar, A., Roy, R., Sherwen, T., Cuevas, C., Saiz-  
578 Lopez, A., Ram, K., & Mahajan, A. S. (2020). Estimation of reactive inorganic iodine  
579 fluxes in the Indian and Southern Ocean marine boundary layer. *Atmospheric Chemistry  
and Physics*, 20(20), 12093–12114. <https://doi.org/10.5194/acp-20-12093-2020>
- 580 Inness, A., Ades, M., Agustí-Panareda, A., Barré, J., Benedictow, A., Blechschmidt, A.-M.,  
581 Dominguez, J. J., Engelen, R., Eskes, H., Flemming, J., Huijnen, V., Jones, L., Kipling,  
582 Z., Massart, S., Parrington, M., Peuch, V.-H., Razinger, M., Remy, S., Schulz, M., &  
583 Suttie, M. (2019). The CAMS reanalysis of atmospheric composition. *Atmospheric  
Chemistry and Physics*, 19(6), 3515–3556. <https://doi.org/10.5194/acp-19-3515-2019>
- 584
- 585

- 586 Jones, C. E., Hornsby, K. E., Sommariva, R., Dunk, R. M., von Glasow, R., McFiggans, G., &  
587 Carpenter, L. J. (2010). Quantifying the contribution of marine organic gases to  
588 atmospheric iodine. *Geophysical Research Letters*, 37(18).  
589 <https://doi.org/10.1029/2010GL043990>
- 590 Koenig, T. K., Baidar, S., Campuzano-Jost, P., Cuevas, C. A., Dix, B., Fernandez, R. P., Guo,  
591 H., Hall, S. R., Kinnison, D., Nault, B. A., Ullmann, K., Jimenez, J. L., Saiz-Lopez, A., &  
592 Volkamer, R. (2020). Quantitative detection of iodine in the stratosphere. *Proceedings of  
593 the National Academy of Sciences*, 117(4), 1860–1866.  
594 <https://doi.org/10.1073/pnas.1916828117>
- 595 Koenig, T. K., Volkamer, R., Apel, E. C., Bresch, J. F., Cuevas, C. A., Dix, B., Eloranta, E. W.,  
596 Fernandez, R. P., Hall, S. R., Hornbrook, R. S., Pierce, R. B., Reeves, J. M., Saiz-Lopez,  
597 A., & Ullmann, K. (2021). Ozone depletion due to dust release of iodine in the free  
598 troposphere. *Science Advances*, 7(52), 6544. <https://doi.org/10.1126/sciadv.abj6544>
- 599 Lee, C. F., Elgiar, T., David, L. M., Wilmot, K., Reza, M., Hirshorn, N., McCubbin, I. B., Shah,  
600 V., Lin, J. C., Lyman, S. N., Hallar, A. G., Gratz, L. E., & Volkamer, R. (2024).  
601 Measurements and model simulations of iodine monoxide (IO) radical, water vapor  
602 ( $\text{H}_2\text{O}$ ), nitrogen dioxide ( $\text{NO}_2$ ) radical, formaldehyde ( $\text{HCHO}$ ), gaseous elemental  
603 mercury ( $\text{Hg}^{\text{0}}$ ), and oxidized mercury ( $\text{Hg}^{\text{II}}$ ) at Storm Peak Laboratory, Colorado, during  
604 April 2022 (Version 1) [Dataset]. Zenodo. <https://doi.org/10.5281/zenodo.10805550>
- 605 Lee, C. F., Wilmot, K., Lin, J. C., Lyman, S. N., Hallar, A. G., Gratz, L. E., & Volkamer, R.  
606 (2024). 24-hour HYSPLIT-STILT back-trajectories initialized at Storm Peak Laboratory,  
607 Colorado from April 1, 2022 to May 1, 2022 (Version 1) [Dataset]. Zenodo.  
608 <https://doi.org/10.5281/zenodo.10806478>

- 609 Legrand, M., McConnell, J. R., Preunkert, S., Arienzo, M., Chellman, N., Gleason, K., Sherwen,  
610 T., Evans, M. J., & Carpenter, L. J. (2018). Alpine ice evidence of a three-fold increase in  
611 atmospheric iodine deposition since 1950 in Europe due to increasing oceanic emissions.  
612 *Proceedings of the National Academy of Sciences*, 115(48), 12136–12141.  
613 <https://doi.org/10.1073/pnas.1809867115>
- 614 Lin, J. C., Gerbig, C., Wofsy, S. C., Andrews, A. E., Daube, B. C., Davis, K. J., & Grainger, C.  
615 A. (2003). A near-field tool for simulating the upstream influence of atmospheric  
616 observations: The Stochastic Time-Inverted Lagrangian Transport (STILT) model.  
617 *Journal of Geophysical Research: Atmospheres*, 108(D16).  
618 <https://doi.org/10.1029/2002JD003161>
- 619 Loughner, C. P., Fasoli, B., Stein, A. F., & Lin, J. C. (2021). Incorporating features from the  
620 Stochastic Time-Inverted Lagrangian Transport (STILT) model into the Hybrid Single-  
621 Particle Lagrangian Integrated Trajectory (HYSPPLIT) model: a unified dispersion model  
622 for time-forward and time-reversed applications. *Journal of Applied Meteorology and*  
623 *Climatology*, 60(6), 799–810. <https://doi.org/10.1175/JAMC-D-20-0158.1>
- 624 Lyman, S. N., Gratz, L. E., Dunham-Cheatham, S. M., Gustin, M. S., & Luippold, A. (2020).  
625 Improvements to the Accuracy of Atmospheric Oxidized Mercury Measurements.  
626 *Environmental Science & Technology*, 54(21), 13379–13388.  
627 <https://doi.org/10.1021/acs.est.0c02747>
- 628 MacDonald, S. M., Gómez Martín, J. C., Chance, R., Warriner, S., Saiz-Lopez, A., Carpenter, L.  
629 J., & Plane, J. M. C. (2014). A laboratory characterisation of inorganic iodine emissions  
630 from the sea surface: dependence on oceanic variables and parameterisation for global

- 631 modelling. *Atmospheric Chemistry and Physics*, 14(11), 5841–5852.
- 632 <https://doi.org/10.5194/acp-14-5841-2014>
- 633 Mahajan, A. S., Gómez Martín, J. C., Hay, T. D., Royer, S.-J., Yvon-Lewis, S., Liu, Y., Hu, L.,  
634 Prados-Roman, C., Ordóñez, C., Plane, J. M. C., & Saiz-Lopez, A. (2012). Latitudinal  
635 distribution of reactive iodine in the Eastern Pacific and its link to open ocean sources.  
636 *Atmospheric Chemistry and Physics*, 12(23), 11609–11617. <https://doi.org/10.5194/acp-12-11609-2012>
- 638 Mahajan, A. S., Shaw, M., Oetjen, H., Hornsby, K. E., Carpenter, L. J., Kaleschke, L., Tian-  
639 Kunze, X., Lee, J. D., Moller, S. J., Edwards, P., Commane, R., Ingham, T., Heard, D. E.,  
640 & Plane, J. M. C. (2010). Evidence of reactive iodine chemistry in the Arctic boundary  
641 layer. *Journal of Geophysical Research: Atmospheres*, 115(D20).  
642 <https://doi.org/10.1029/2009JD013665>
- 643 Miller, M. B., Dunham-Cheatham, S. M., Gustin, M. S., & Edwards, G. C. (2019). Evaluation of  
644 cation exchange membrane performance under exposure to high  $\text{Hg}^0$  and  $\text{HgBr}^2$   
645 concentrations. *Atmospheric Measurement Techniques*, 12(2), 1207–1217.  
646 <https://doi.org/10.5194/amt-12-1207-2019>
- 647 Murphy, D. M., Hudson, P. K., Thomson, D. S., Sheridan, P. J., & Wilson, J. C. (2006).  
648 Observations of Mercury-Containing Aerosols. *Environmental Science & Technology*,  
649 40(10), 3163–3167. <https://doi.org/10.1021/es052385x>
- 650 Obrist, D., Hallar, A. G., McCubbin, I., Stephens, B. B., & Rahn, T. (2008). Atmospheric  
651 mercury concentrations at Storm Peak Laboratory in the Rocky Mountains: Evidence for  
652 long-range transport from Asia, boundary layer contributions, and plant mercury uptake.  
653 *Atmospheric Environment*, 42(33), 7579–7589.

- 654 O'Dowd, C. D., Jimenez, J. L., Bahreini, R., Flagan, R. C., Seinfeld, J. H., Hämeri, K., Pirjola,  
655 L., Kulmala, M., Jennings, S. G., & Hoffmann, T. (2002). Marine aerosol formation from  
656 biogenic iodine emissions. *Nature*, 417(6889), 632–636.  
657 <https://doi.org/10.1038/nature00775>
- 658 Ordóñez, C., Lamarque, J.-F., Tilmes, S., Kinnison, D. E., Atlas, E. L., Blake, D. R., Sousa  
659 Santos, G., Brasseur, G., & Saiz-Lopez, A. (2012). Bromine and iodine chemistry in a  
660 global chemistry-climate model: description and evaluation of very short-lived oceanic  
661 sources. *Atmospheric Chemistry and Physics*, 12(3), 1423–1447.  
662 <https://doi.org/10.5194/acp-12-1423-2012>
- 663 Ortega, I., Berg, L. K., Ferrare, R. A., Hair, J. W., Hostetler, C. A., & Volkamer, R. (2016).  
664 Elevated aerosol layers modify the O<sub>2</sub>–O<sub>2</sub> absorption measured by ground-based MAX-  
665 DOAS. *Journal of Quantitative Spectroscopy and Radiative Transfer*, 176, 34–49.  
666 <https://doi.org/10.1016/j.jqsrt.2016.02.021>
- 667 Platt, U. & Stutz, J. (2008). Differential Optical Absorption Spectroscopy: Principles and  
668 Applications. Berlin, Germany: Springer. <https://doi.org/10.1007/978-3-540-75776-4>
- 669 Prados-Roman, C., Cuevas, C. A., Hay, T., Fernandez, R. P., Mahajan, A. S., Royer, S.-J., Galí,  
670 M., Simó, R., Dachs, J., Großmann, K., Kinnison, D. E., Lamarque, J.-F., & Saiz-Lopez,  
671 A. (2015). Iodine oxide in the global marine boundary layer. *Atmospheric Chemistry and  
672 Physics*, 15(2), 583–593. <https://doi.org/10.5194/acp-15-583-2015>
- 673 Puentedura, O., Gil, M., Saiz-Lopez, A., Hay, T., Navarro-Comas, M., Gómez-Pelaez, A.,  
674 Cuevas, E., Iglesias, J., & Gomez, L. (2012). Iodine monoxide in the north subtropical  
675 free troposphere. *Atmospheric Chemistry and Physics*, 12(11), 4909–4921.  
676 <https://doi.org/10.5194/acp-12-4909-2012>

- 677 Read, K. A., Mahajan, A. S., Carpenter, L. J., Evans, M. J., Faria, B. V. E., Heard, D. E.,  
678 Hopkins, J. R., Lee, J. D., Moller, S. J., Lewis, A. C., Mendes, L., McQuaid, J. B.,  
679 Oetjen, H., Saiz-Lopez, A., Pilling, M. J., & Plane, J. M. C. (2008). Extensive halogen-  
680 mediated ozone destruction over the tropical Atlantic Ocean. *Nature*, 453(7199), 1232–  
681 1235. <https://doi.org/10.1038/nature07035>
- 682 Rodgers, C.D. (2000). Inverse Methods for Atmospheric Sounding: Theory and Practice.  
683 Singapore: World Scientific Publishing. <https://doi.org/10.1142/3171>
- 684 Saiz-Lopez, A., Fernandez, R. P., Ordóñez, C., Kinnison, D. E., Gómez Martín, J. C., Lamarque,  
685 J.-F., & Tilmes, S. (2014). Iodine chemistry in the troposphere and its effect on ozone.  
686 *Atmospheric Chemistry and Physics*, 14(23), 13119–13143. <https://doi.org/10.5194/acp-14-13119-2014>
- 688 Saiz-Lopez, A., Lamarque, J.-F., Kinnison, D. E., Tilmes, S., Ordóñez, C., Orlando, J. J., Conley,  
689 A. J., Plane, J. M. C., Mahajan, A. S., Sousa Santos, G., Atlas, E. L., Blake, D. R.,  
690 Sander, S. P., Schauffler, S., Thompson, A. M., & Brasseur, G. (2012). Estimating the  
691 climate significance of halogen-driven ozone loss in the tropical marine troposphere.  
692 *Atmospheric Chemistry and Physics*, 12(9), 3939–3949. <https://doi.org/10.5194/acp-12-3939-2012>
- 694 Saiz-Lopez, A., Sitkiewicz, S. P., Roca-Sanjuán, D., Oliva-Enrich, J. M., Dávalos, J. Z., Notario,  
695 R., Jiskra, M., Xu, Y., Wang, F., Thackray, C. P., Sunderland, E. M., Jacob, D. J.,  
696 Travnikov, O., Cuevas, C. A., Acuña, A. U., Rivero, D., Plane, J. M. C., Kinnison, D. E.,  
697 & Sonke, J. E. (2018). Photoreduction of gaseous oxidized mercury changes global  
698 atmospheric mercury speciation, transport and deposition. *Nature Communications*, 9(1),  
699 4796. <https://doi.org/10.1038/s41467-018-07075-3>

- 700 Saiz-Lopez, A., Travnikov, O., Sonke, J. E., Thackray, C. P., Jacob, D. J., Carmona-García, J.,  
701 Francés-Monerris, A., Roca-Sanjuán, D., Acuña, A. U., Dávalos, J. Z., Cuevas, C. A.,  
702 Jiskra, M., Wang, F., Bieser, J., Plane, J. M. C., & Francisco, J. S. (2020).  
703 Photochemistry of oxidized Hg(I) and Hg(II) species suggests missing mercury oxidation  
704 in the troposphere. *Proceedings of the National Academy of Sciences*, 117(49), 30949–  
705 30956. <https://doi.org/10.1073/pnas.1922486117>
- 706 Schönhardt, A., Begoin, M., Richter, A., Wittrock, F., Kaleschke, L., Gómez Martín, J. C., &  
707 Burrows, J. P. (2012). Simultaneous satellite observations of IO and BrO over Antarctica.  
708 *Atmospheric Chemistry and Physics*, 12(14), 6565–6580. <https://doi.org/10.5194/acp-12-6565-2012>
- 710 Schönhardt, A., Richter, A., Theys, N., & Burrows, J. P. (2017). Space-based observation of  
711 volcanic iodine monoxide. *Atmospheric Chemistry and Physics*, 17(7), 4857–4870.  
712 <https://doi.org/10.5194/acp-17-4857-2017>
- 713 Schönhardt, A., Richter, A., Wittrock, F., Kirk, H., Oetjen, H., Roscoe, H. K., & Burrows, J. P.  
714 (2008). Observations of iodine monoxide columns from satellite. *Atmospheric Chemistry  
715 and Physics*, 8(3), 637–653. <https://doi.org/10.5194/acp-8-637-2008>
- 716 Shah, V., Jacob, D. J., Dang, R., Lamsal, L. N., Strode, S. A., Steenrod, S. D., Boersma, K. F.,  
717 Eastham, S. D., Fritz, T. M., Thompson, C., Peischl, J., Bourgeois, I., Pollack, I. B.,  
718 Nault, B. A., Cohen, R. C., Campuzano-Jost, P., Jimenez, J. L., Andersen, S. T.,  
719 Carpenter, L. J., Sherwen, T. J., & Evans, M. J. (2023). Nitrogen oxides in the free  
720 troposphere: implications for tropospheric oxidants and the interpretation of satellite NO<sub>2</sub>  
721 measurements. *Atmospheric Chemistry and Physics*, 23(2), 1227–1257.  
722 <https://doi.org/10.5194/acp-23-1227-2023>

- 723 Shah, V., Jacob, D. J., Thackray, C. P., Wang, X., Sunderland, E. M., Dibble, T. S., Saiz-Lopez,  
724 A., Černušák, I., Kellö, V., Castro, P. J., Wu, R., & Wang, C. (2021). Improved  
725 Mechanistic Model of the Atmospheric Redox Chemistry of Mercury. *Environmental*  
726 *Science & Technology*, 55(21), 14445–14456. <https://doi.org/10.1021/acs.est.1c03160>
- 727 Shepler, B. C., Balabanov, N. B., & Peterson, K. A. (2005). Ab Initio Thermochemistry  
728 Involving Heavy Atoms: An Investigation of the Reactions Hg + IX (X = I, Br, Cl, O).  
729 *The Journal of Physical Chemistry A*, 109(45), 10363–10372.  
730 <https://doi.org/10.1021/jp0541617>
- 731 Sherwen, T., Evans, M. J., Carpenter, L. J., Andrews, S. J., Lidster, R. T., Dix, B., Koenig, T. K.,  
732 Sinreich, R., Ortega, I., Volkamer, R., Saiz-Lopez, A., Prados-Roman, C., Mahajan, A.  
733 S., & Ordóñez, C. (2016a). Iodine's impact on tropospheric oxidants: a global model  
734 study in GEOS-Chem. *Atmospheric Chemistry and Physics*, 16(2), 1161–1186.  
735 <https://doi.org/10.5194/acp-16-1161-2016>
- 736 Sherwen, T., Evans, M. J., Carpenter, L. J., Schmidt, J. A., & Mickley, L. J. (2017). Halogen  
737 chemistry reduces tropospheric O<sub>3</sub> radiative forcing. *Atmospheric Chemistry and Physics*,  
738 17(2), 1557–1569. <https://doi.org/10.5194/acp-17-1557-2017>
- 739 Sherwen, T., Schmidt, J. A., Evans, M. J., Carpenter, L. J., Großmann, K., Eastham, S. D., Jacob,  
740 D. J., Dix, B., Koenig, T. K., Sinreich, R., Ortega, I., Volkamer, R., Saiz-Lopez, A.,  
741 Prados-Roman, C., Mahajan, A. S., & Ordóñez, C. (2016b). Global impacts of  
742 tropospheric halogens (Cl, Br, I) on oxidants and composition in GEOS-Chem.  
743 *Atmospheric Chemistry and Physics*, 16(18), 12239–12271. <https://doi.org/10.5194/acp-16-12239-2016>

- 745 Sipilä, M., Sarnela, N., Jokinen, T., Henschel, H., Junninen, H., Kontkanen, J., Richters, S.,  
746 Kangasluoma, J., Franchin, A., Peräkylä, O., Rissanen, M. P., Ehn, M., Vehkamäki, H.,  
747 Kurten, T., Berndt, T., Petäjä, T., Worsnop, D., Ceburnis, D., Kerminen, V.-M., Kulmala,  
748 M., & O'Dowd, C. (2016). Molecular-scale evidence of aerosol particle formation via  
749 sequential addition of  $\text{HIO}_3$ . *Nature*, 537(7621), 532–534.  
750 <https://doi.org/10.1038/nature19314>
- 751 Sive, B. C., Varner, R. K., Mao, H., Blake, D. R., Wingenter, O. W., & Talbot, R. (2007). A  
752 large terrestrial source of methyl iodide. *Geophysical Research Letters*, 34(17).  
753 <https://doi.org/10.1029/2007GL030528>
- 754 Spietz, P., Gómez Martín, J. C., & Burrows, J. P. (2005). Spectroscopic studies of the  $\text{I}_2/\text{O}_3$   
755 photochemistry. *Journal of Photochemistry and Photobiology A: Chemistry*, 176(1–3),  
756 50–67. <https://doi.org/10.1016/j.jphotochem.2005.08.023>
- 757 Spinei, E., Cede, A., Herman, J., Mount, G. H., Eloranta, E., Morley, B., Baidar, S., Dix, B.,  
758 Ortega, I., Koenig, T., & Volkamer, R. (2015). Ground-based direct-sun DOAS and  
759 airborne MAX-DOAS measurements of the collision-induced oxygen complex,  $\text{O}_2\text{O}_2$ ,  
760 absorption with significant pressure and temperature differences. *Atmospheric  
761 Measurement Techniques*, 8(2), 793–809. <https://doi.org/10.5194/amt-8-793-2015>
- 762 Takashima, H., Kanaya, Y., Kato, S., Friedrich, M. M., van Roozendael, M., Taketani, F.,  
763 Miyakawa, T., Komazaki, Y., Cuevas, C. A., Saiz-Lopez, A., & Sekiya, T. (2022). Full  
764 latitudinal marine atmospheric measurements of iodine monoxide. *Atmospheric  
765 Chemistry and Physics*, 22(6), 4005–4018. <https://doi.org/10.5194/acp-22-4005-2022>
- 766 Tirpitz, J.-L., Frieß, U., Hendrick, F., Alberti, C., Allaart, M., Apituley, A., Bais, A., Beirle, S.,  
767 Berkhouit, S., Bognar, K., Bösch, T., Bruchkouski, I., Cede, A., Chan, K. L., den Hoed,

- 768 M., Donner, S., Drosoglou, T., Fayt, C., Friedrich, M. M., Frumau, A., Gast, L., Gielen,  
769 C., Gomez-Martín, L., Hao, N., Hensen, A., Henzing, B., Hermans, C., Jin, J., Kreher, K.,  
770 Kuhn, J., Lampel, J., Li, A., Liu, C., Liu, H., Ma, J., Merlaud, A., Peters, E., Pinardi, G.,  
771 Piters, A., Platt, U., Puentedura, O., Richter, A., Schmitt, S., Spinei, E., Stein Zweers, D.,  
772 Strong, K., Swart, D., Tack, F., Tiefengraber, M., van der Hoff, R., van Roozendael, M.,  
773 Vlemmix, T., Vonk, J., Wagner, T., Wang, Y., Wang, Z., Wenig, M., Wiegner, M.,  
774 Witrock, F., Xie, P., Xing, C., Xu, J., Yela, M., Zhang, C., & Zhao, X. (2021).  
775 Intercomparison of MAX-DOAS vertical profile retrieval algorithms: studies on field  
776 data from the CINDI-2 campaign. *Atmospheric Measurement Techniques*, 14(1), 1–35.  
777 <https://doi.org/10.5194/amt-14-1-2021>
- 778 Van Roozendael, M., & the DOAS UV-VIS team at BIRA-IASB (2017). QDOAS: January 21,  
779 2021 Release (version 3.4.5) [Software]. Royal Belgian Institute for Space Aeronomy.  
780 <https://uv-vis.aeronomie.be/software/QDOAS/index.php> (retrieved April 22, 2021)
- 781 Volkamer, R., Baidar, S., Campos, T. L., Coburn, S., DiGangi, J. P., Dix, B., Eloranta, E. W.,  
782 Koenig, T. K., Morley, B., Ortega, I., Pierce, B. R., Reeves, M., Sinreich, R., Wang, S.,  
783 Zondlo, M. A., & Romashkin, P. A. (2015). Aircraft measurements of BrO, IO, glyoxal,  
784 NO<sub>2</sub>, H<sub>2</sub>O, O<sub>2</sub>–O<sub>2</sub> and aerosol extinction profiles in the tropics: comparison with aircraft-  
785 /ship-based in situ and lidar measurements. *Atmospheric Measurement Techniques*, 8(5),  
786 2121–2148. <https://doi.org/10.5194/amt-8-2121-2015>
- 787 Wagner, T., Apituley, A., Beirle, S., Dörner, S., Friess, U., Remmers, J., & Shaiganfar, R.  
788 (2014). Cloud detection and classification based on MAX-DOAS observations.  
789 *Atmospheric Measurement Techniques*, 7(5), 1289–1320. <https://doi.org/10.5194/amt-7-1289-2014>

- 791 Wagner, T., Beirle, S., Benavent, N., Bösch, T., Chan, K. L., Donner, S., Dörner, S., Fayt, C.,  
792 Frieß, U., García-Nieto, D., Gielen, C., González-Bartolome, D., Gomez, L., Hendrick,  
793 F., Henzing, B., Jin, J. L., Lampel, J., Ma, J., Mies, K., Navarro, M., Peters, E., Pinardi,  
794 G., Puentedura, O., Pukīte, J., Remmers, J., Richter, A., Saiz-Lopez, A., Shaiganfar, R.,  
795 Sihler, H., Van Roozendael, M., Wang, Y., & Yela, M. (2019). Is a scaling factor  
796 required to obtain closure between measured and modelled atmospheric O<sub>4</sub> absorptions?  
797 An assessment of uncertainties of measurements and radiative transfer simulations for 2  
798 selected days during the MAD-CAT campaign. *Atmospheric Measurement Techniques*,  
799 12(5), 2745–2817. <https://doi.org/10.5194/amt-12-2745-2019>
- 800 Wang, X., Jacob, D. J., Downs, W., Zhai, S., Zhu, L., Shah, V., Holmes, C. D., Sherwen, T.,  
801 Alexander, B., Evans, M. J., Eastham, S. D., Neuman, J. A., Veres, P. R., Koenig, T. K.,  
802 Volkamer, R., Huey, L. G., Bannan, T. J., Percival, C. J., Lee, B. H., & Thornton, J. A.  
803 (2021). Global tropospheric halogen (Cl, Br, I) chemistry and its impact on oxidants.  
804 *Atmospheric Chemistry and Physics*, 21(18), 13973–13996. <https://doi.org/10.5194/acp-21-13973-2021>
- 805 Wang, S., Schmidt, J. A., Baidar, S., Coburn, S., Dix, B., Koenig, T. K., Apel, E., Bowdalo, D.,  
806 Campos, T. L., Eloranta, E., Evans, M. J., DiGangi, J. P., Zondlo, M. A., Gao, R.-S.,  
807 Haggerty, J. A., Hall, S. R., Hornbrook, R. S., Jacob, D., Morley, B., Pierce, B., Reevesj,  
808 M., Romashkin, P., ter Schure, A., Volkamer, R. (2015). Active and widespread halogen  
809 chemistry in the tropical and subtropical free troposphere. *Proceedings of the National  
810 Academy of Sciences*, 112(30), 9281–9286. <https://doi.org/10.1073/pnas.1505142112>
- 811 Wennberg, P. O., Brault, J. W., Hanisco, T. F., Salawitch, R. J., & Mount, G. H. (1997). The  
812 atmospheric column abundance of IO: Implications for stratospheric ozone. *Journal of*

- 814        *Geophysical Research: Atmospheres*, 102(D7), 8887–8898.
- 815        <https://doi.org/10.1029/96JD03712>
- 816        Whalley, L. K., Furneaux, K. L., Gravestock, T., Atkinson, H. M., Bale, C. S. E., Ingham, T.,
- 817        Bloss, W. J., & Heard, D. E. (2007). Detection of iodine monoxide radicals in the marine
- 818        boundary layer using laser induced fluorescence spectroscopy. *Journal of Atmospheric*
- 819        *Chemistry*, 58(1), 19–39. <https://doi.org/10.1007/s10874-007-9075-9>
- 820        Williams, J., Gros, V., Atlas, E., Maciejczyk, K., Batsaikhan, A., Schöler, H. F., Forster, C.,
- 821        Quack, B., Yassaa, N., Sander, R., & van Dingenen, R. (2007). Possible evidence for a
- 822        connection between methyl iodide emissions and Saharan dust. *Journal of Geophysical*
- 823        *Research: Atmospheres*, 112(D7). <https://doi.org/10.1029/2005JD006702>
- 824        Wittrock, F., Müller, R., Richter, A., Bovensmann, H., & Burrows, J. P. (2000). Measurements
- 825        of iodine monoxide (IO) above Spitsbergen. *Geophysical Research Letters*, 27(10),
- 826        1471–1474. <https://doi.org/10.1029/1999GL011146>
- 827        Wolfe, G. M., Marvin, M. R., Roberts, S. J., Travis, K. R., & Liao, J. (2016). The Framework for
- 828        0-D Atmospheric Modeling (F0AM) v3.1. *Geoscientific Model Development*, 9(9), 3309–
- 829        3319. <https://doi.org/10.5194/gmd-9-3309-2016>
- 830        Zhao, X., Hou, X., & Zhou, W. (2019). Atmospheric Iodine ( $^{127}\text{I}$  and  $^{129}\text{I}$ ) Record in Spruce Tree
- 831        Rings in the Northeast Qinghai-Tibet Plateau. *Environmental Science & Technology*,
- 832        53(15), 8706–8714. <https://doi.org/10.1021/acs.est.9b01160>
- 833
- 834        **References From the Supporting Information**
- 835        Chance, K., & Kurucz, R. L. (2010). An improved high-resolution solar reference spectrum for
- 836        earth's atmosphere measurements in the ultraviolet, visible, and near infrared. *Journal of*

- 837        *Quantitative Spectroscopy and Radiative Transfer*, 111(9), 1289–1295.
- 838        <https://doi.org/10.1016/j.jqsrt.2010.01.036>
- 839        Dowell, D. C., Alexander, C. R., James, E. P., Weygandt, S. S., Benjamin, S. G., Manikin, G. S.,  
840           Blake, B. T., Brown, J. M., Olson, J. B., Hu, M., Smirnova, T. G., Ladwig, T., Kenyon, J.  
841           S., Ahmadov, R., Turner, D. D., Duda, J. D., & Alcott, T. I. (2022). The High-Resolution  
842           Rapid Refresh (HRRR): An Hourly Updating Convection-Allowing Forecast Model. Part  
843           I: Motivation and System Description. *Weather and Forecasting*, 37(8), 1371–1395.  
844        <https://doi.org/10.1175/WAF-D-21-0151.1>
- 845        Fleischmann, O. C., Hartmann, M., Burrows, J. P., & Orphal, J. (2004). New ultraviolet  
846           absorption cross-sections of BrO at atmospheric temperatures measured by time-  
847           windowing Fourier transform spectroscopy. *Journal of Photochemistry and Photobiology*  
848           A: Chemistry, 168(1–2), 117–132. <https://doi.org/10.1016/j.jphotochem.2004.03.026>
- 849        Giglio, L., Randerson, J. T., & van der Werf, G. R. (2013). Analysis of daily, monthly, and  
850           annual burned area using the fourth-generation global fire emissions database (GFED4).  
851        *Journal of Geophysical Research: Biogeosciences*, 118(1), 317–328.  
852        <https://doi.org/10.1002/jgrg.20042>
- 853        Guenther, A. B., Jiang, X., Heald, C. L., Sakulyanontvittaya, T., Duhl, T., Emmons, L. K., &  
854           Wang, X. (2012). The Model of Emissions of Gases and Aerosols from Nature version  
855           2.1 (MEGAN2.1): an extended and updated framework for modeling biogenic emissions.  
856        *Geoscientific Model Development*, 5(6), 1471–1492. <https://doi.org/10.5194/gmd-5-1471-2012>
- 858        Hoesly, R. M., Smith, S. J., Feng, L., Klimont, Z., Janssens-Maenhout, G., Pitkanen, T., Seibert,  
859           J. J., Vu, L., Andres, R. J., Bolt, R. M., Bond, T. C., Dawidowski, L., Kholod, N.,

- 860 Kurokawa, J., Li, M., Liu, L., Lu, Z., Moura, M. C. P., O'Rourke, P. R., & Zhang, Q.  
861 (2018). Historical (1750–2014) anthropogenic emissions of reactive gases and aerosols  
862 from the Community Emissions Data System (CEDS). *Geoscientific Model Development*,  
863 11(1), 369–408. <https://doi.org/10.5194/gmd-11-369-2018>
- 864 Finkenzeller, H., & Volkamer, R. (2022). O<sub>2</sub>–O<sub>2</sub> CIA in the gas phase: Cross-section of weak  
865 bands, and continuum absorption between 297–500 nm. *Journal of Quantitative  
866 Spectroscopy and Radiative Transfer*, 279, 108063.  
867 <https://doi.org/10.1016/j.jqsrt.2021.108063>
- 868 Lampel, J., Frieß, U., & Platt, U. (2015). The  
869 impact of vibrational Raman scattering of air on DOAS measurements of atmospheric  
870 trace gases. *Atmospheric Measurement Techniques*, 8(9), 3767–3787.  
871 <https://doi.org/10.5194/amt-8-3767-2015>
- 872 Meller, R., & Moortgat, G. K. (2000). Temperature dependence of the absorption cross sections  
873 of formaldehyde between 223 and 323 K in the wavelength range 225–375 nm. *Journal  
874 of Geophysical Research: Atmospheres*, 105(D6), 7089–7101.  
875 <https://doi.org/10.1029/1999JD901074>
- 876 Pukīte, J., & Wagner, T. (2016). Quantification and parametrization of non-linearity effects by  
877 higher-order sensitivity terms in scattered light differential optical absorption  
878 spectroscopy. *Atmospheric Measurement Techniques*, 9(5), 2147–2177.  
879 <https://doi.org/10.5194/amt-9-2147-2016>
- 880 Rothman, L. S., Gordon, I. E., Babikov, Y., Barbe, A., Chris Benner, D., Bernath, P. F., Birk,  
881 M., Bizzocchi, L., Boudon, V., Brown, L. R., Campargue, A., Chance, K., Cohen, E. A.,  
882 Coudert, L. H., Devi, V. M., Drouin, B. J., Fayt, A., Flaud, J.-M., Gamache, R. R.,  
Harrison, J. J., Hartmann, J.-M., Hill, C., Hodges, J. T., Jacquemart, D., Jolly, A.,

- 883 Lamouroux, J., Le Roy, R. J., Li, G., Long, D. A., Lyulin, O. M., Mackie, C. J., Massie,  
884 S. T., Mikhailenko, S., Müller, H. S. P., Naumenko, O.V., Nikitin, A.V., Orphal, J.,  
885 Perevalov, V., Perrin, A., Polovtseva, E. R., Richard, C., Smith, M. A. H., Starikova, E.,  
886 Sung, K., Tashkun, S., Tennyson, J., Toon, G.C., Tyuterev, Vl. G., & Wagner, G. (2013).  
887 The HITRAN2012 molecular spectroscopic database. *Journal of Quantitative*  
888 *Spectroscopy and Radiative Transfer*, 130, 4–50.  
889 <https://doi.org/10.1016/j.jqsrt.2013.07.002>
- 890 Rothman, L. S., Gordon, I. E., Barber, R. J., Dothe, H., Gamache, R. R., Goldman, A.,  
891 Perevalov, V. I., Tashkun, S. A., & Tennyson, J. (2010). HITEMP, the high-temperature  
892 molecular spectroscopic database. *Journal of Quantitative Spectroscopy and Radiative*  
893 *Transfer*, 111(15), 2139–2150. <https://doi.org/10.1016/j.jqsrt.2010.05.001>
- 894 Serdyuchenko, A., Gorshelev, V., Weber, M., Chehade, W., & Burrows, J. P. (2014). High  
895 spectral resolution ozone absorption cross-sections – Part 2: Temperature dependence.  
896 *Atmospheric Measurement Techniques*, 7(2), 625–636. <https://doi.org/10.5194/amt-7-625-2014>
- 898 Thalman, R., & Volkamer, R. (2013). Temperature dependent absorption cross-sections of O<sub>2</sub>–  
899 O<sub>2</sub> collision pairs between 340 and 630 nm and at atmospherically relevant pressure.  
900 *Physical Chemistry Chemical Physics*, 15(37), 15371.  
901 <https://doi.org/10.1039/c3cp50968k>
- 902 Vandaele, A. C., Hermans, C., Simon, P. C., Carleer, M., Colin, R., Fally, S., Mérienne, M. F.,  
903 Jenouvrier, A., & Coquart, B. (1998). Measurements of the NO<sub>2</sub> absorption cross-section  
904 from 42 000 cm<sup>-1</sup> to 10 000 cm<sup>-1</sup> (238–1000 nm) at 220 K and 294 K. *Journal of*

905      *Quantitative Spectroscopy and Radiative Transfer*, 59(3–5), 171–184.

906      [https://doi.org/10.1016/S0022-4073\(97\)00168-4](https://doi.org/10.1016/S0022-4073(97)00168-4)